Politecnico di Torino

Politecnico di Torino

Master Degree in Environmental and Land Engineering, Climate change

Academic year 2024/2025

November 2025

Response of ENSO variability to reduced AMOC strength

Supervisor:
Prof. Jost-Diedrich Graf Von Hardenberg

Co-supervisor:
Prof. Katinka Bellomo

Candidate:
Alessia Dellea

Abstract

The El Niño-Southern Oscillation (ENSO) and the Atlantic Meridional Overturning Circulation (AMOC) are critical components of the global climate system. Their potential interaction through teleconnections is a subject of major scientific importance, yet existing literature lacks consensus on the nature of this link, especially under future warming scenarios.

This thesis investigates the state dependence of the AMOC-ENSO teleconnection, examining how their interaction changes based on the background climate state. Using the EC-Earth3 climate model, four targeted simulations are analyzed: a strong and weak AMOC state under both preindustrial and high-emission 4xCO_2 conditions.

Under preindustrial conditions, a weakened AMOC induces a weak and asymmetric response. The net effect on ENSO variability is minimal, with a modest amplification of El Niño events in the eastern Pacific, while La Niña events remain largely unchanged. The dynamics shift fundamentally in the 4xCO_2 climate. The analysis first isolates the impact of greenhouse forcing, revealing that a 4xCO_2 scenario with a strong AMOC acts as a strong amplifier of ENSO, producing more intense events and a pronounced westward shift of their spatial footprint. The key finding emerges when a weakened AMOC is introduced into this warmer world. In this context, the AMOC slowdown acts as a negative feedback, partially offsetting the greenhouse-gas-driven intensification of ENSO and reversing its westward expansion, forcing the variability pattern back toward a more canonical, Eastern-Pacific-focused structure.

The main conclusion is that the AMOC-ENSO teleconnection is strongly state-dependent. Its role transforms from a marginal amplifier in a preindustrial world to a significant modulator that opposes the primary effects of greenhouse forcing in a high-CO_2 climate. This implies that future projections of ENSO and its global impacts cannot be considered reliable without accounting for the concurrent, and widely projected, slowdown of the AMOC.

Table of Contents

List of Figures

Chapter 1

Introduction

1.1 El Niño Southern Oscillation (ENSO)

The El Niño-Southern Oscillation (ENSO) is a naturally occurring climate phenomenon resulting from complex interactions between the tropical Pacific Ocean and the overlying atmosphere. It represents a coupled ocean-atmosphere mode of variability, sustained by internal feedbacks involving sea surface temperature (SST), atmospheric convection, trade winds, and large-scale pressure gradients. Although ENSO originates in the equatorial Pacific, its climatic influence extends worldwide, making it one of the most prominent sources of interannual variability in the global climate system.

ENSO is not a single event but a recurring cycle that oscillates between three phases: El Niño, La Niña, and neutral conditions. These events alternate irregularly every 2 to 7 years and are defined by characteristic anomalies in SSTs and atmospheric circulation. El Niño and La Niña represent opposite states of the system and occur when critical thresholds in SST, trade winds, and pressure gradient are exceeded (Trenberth, 1997).

Historically, the term "El Niño" referred to the periodic warming of coastal waters off Ecuador and Peru around Christmas time. In modern climatology, however, it describes the broader phenomenon of unusual warming of SSTs across the central and eastern equatorial Pacific. El Niño events are usually linked with weakened or even reversed easterly trade winds, a flattened thermocline, and reduced upwelling

of cold, nutrient-rich waters along the South American coast. Conversely, La Niña events are characterized by unusually cool SSTs, stronger easterly winds, a steeper thermocline, and increased upwelling in the eastern Pacific. Generally, La Niña events tend to be somewhat weaker but more prolonged than El Niño episodes (Okumura & Deser, 2010).

The atmospheric counterpart of ENSO, known as the Southern Oscillation, was first described by Gilbert Walker in the early 20^{th} century. It refers to a large-scale oscillation in surface air pressure between the western and eastern tropical Pacific. Its intensity is commonly quantified by the Southern Oscillation Index (SOI), which measures the difference in sea level pressure between Tahiti and Darwin, Australia. Negative SOI values reflect weakened pressure gradients and trade winds, typically favoring El Niño development, whereas positive SOI values indicate stronger easterlies and the onset of La Niña conditions (Power & Kociuba, 2010).

The coupled ocean-atmosphere mechanism underlying ENSO was formalized by Bjerknes (1969), who linked Walker's observations of atmospheric pressure changes to fluctuations in Pacific SSTs. This relationship forms the basis of the Bjerknes feedback, a positive feedback loop in which oceanic and atmospheric anomalies mutually reinforce each other. Under neutral conditions, warm SSTs in the western Pacific promote deep atmospheric convection that reinforces the easterly trade winds. These winds drive surface waters westward, maintaining the zonal SST gradient and supporting cold water upwelling in the east. When trade winds weaken, due to internal variability or external forcing, warm surface waters can shift eastward, flattening the thermocline and relocating convection toward the central and eastern Pacific. This further weakens the winds, completing a self-reinforcing cycle that can potentially evolve into an El Niño event. La Niña represents the opposite state, with intensified trade winds enhancing upwelling in the east, steepening the SST gradient, and strengthening convection over the western Pacific (Stewart, 2008; Wang et al., 2017).

Figure 1.1 illustrates the contrasting oceanic and atmospheric states during La Niña, neutral, and El Niño phases along the equatorial Pacific.

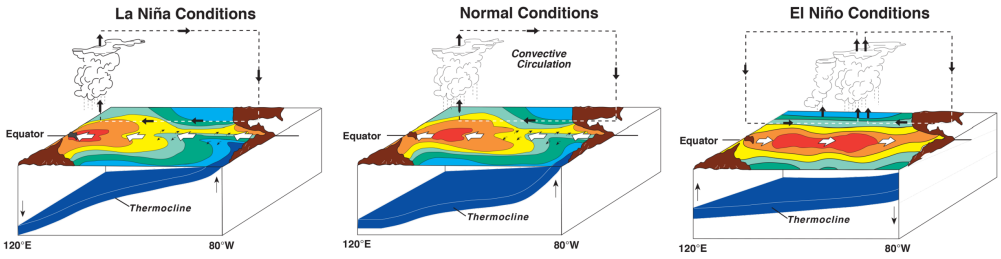

Figure 1.1: Schematic diagram showing the atmospheric and oceanic conditions along the equator in La Niña, Normal, and El Niño conditions. Source: NOAA PMEL.

One of the most important features of ENSO is its ability to generate widespread, and often predictable, climate anomalies far from its Pacific origins (Alexander et al., 2002). These teleconnections arise primarily through ENSO's modulation of tropical convection and the associated release of latent heat, which alter atmospheric circulation on a global scale. For example, during El Niño years, enhanced convection and rainfall shift eastward across the Pacific, redistributing heat in the upper atmosphere and altering jet stream paths. These teleconnections can result in profound disruptions to temperature and precipitation patterns across the globe, often with substantial socio-economic consequences. For instance, the 2015-2016 El Niño event affected more than 60 million people worldwide, leading to widespread food insecurity, displacement, and public health emergencies (OCHA, 2017).
Regionally, El Niño events tend to produce increased rainfall in the central Pacific, eastern Africa, and western South America, while drought conditions often emerge over Australia, Indonesia, parts of South Asia, and northeastern South America. La Niña generally produces the opposite effects, with enhanced precipitation in the western Pacific and drier conditions in the central and eastern basin (Ropelewski & Halpert, 1987). ENSO also contributes to short-term variations in the global mean temperature (Lean & Rind, 2008).
In recent decades, it has become evident that ENSO exhibits more diversity than the canonical Eastern Pacific (EP) El Niño events. A particularly well-studied variant is the Central Pacific (CP) El Niño, also known as El Niño Modoki, characterized by warming anomalies centered closer to the dateline rather than off the South American coast (C. Wang et al., 2017). These non-canonical events produce distinct teleconnection patterns and consequently different climate impacts (Ashok et al.,

2007), highlighting the evolving complexity of ENSO dynamics in the context of natural variability and external forcing. While some authors argue that ENSO should be understood as a continuous spectrum rather than distinct types (Capotondi et al., 2015; Johnson, 2013), the CP-EP classification remains widely used in the literature.

1.2 Impacts of climate change on ENSO

Given its central role in influencing global climate variability, understanding ENSO's response to ongoing anthropogenic climate change and its potential evolution under future warming is of critical scientific and societal relevance. ENSO arises from delicate ocean-atmosphere feedbacks in the tropical Pacific, meaning that even subtle changes in the mean state of the climate system may profoundly influence its amplitude, frequency and spatial pattern. One of the key challenges in climate science today lies in determining whether ENSO behavior has already been altered by human-induced climate change, and if so, to what extent. Equally pressing is the question of how ENSO characteristics may transform as global warming continues to intensify.

This subject remains an area of active research, marked by limited consensus within the scientific community. ENSO is inherently nonlinear and complex, governed by interacting feedbacks that are not yet fully understood. Moreover, the instrumental record, spanning only a few decades with reliable coverage, is relatively short, complicating the effort to distinguish between natural variability and forced trends. According to the IPCC Sixth Assessment Report (2023), there is currently no clear evidence that anthropogenic climate change has significantly modified ENSO-related SST anomalies in the tropical Pacific. However, more recent studies suggest that such an influence may already be emerging.

One of the most consistent indications of an evolving ENSO system is an observed increase in the amplitude of SST variability within its core region over the past five to six decades (Figure 1.2). This trend suggests a potentially more energetic ENSO system, characterized by intensified alternation between El Niño and La Niña phases. Although it remains difficult to attribute these changes unequivocally to anthropogenic forcing, the physical mechanisms linking greenhouse gas emissions

to enhanced ENSO variability are plausible, given that atmospheric greenhouse gas levels have increased by approximately 50% since preindustrial times (Lan et al., 2025), altering the Earth's energy balance and influencing ocean-atmosphere interactions.

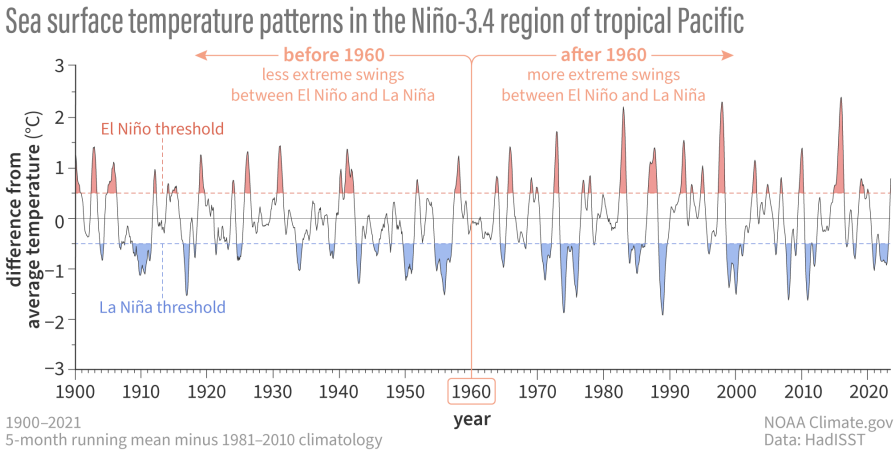

Figure 1.2: SST anomalies during El Niño and La Niña events from 1900 to 2020. Source: NOAA.

In this context, Cai et al. (2023) have analyzed historical records and conducted multi-century climate model simulations, finding that ENSO variability may have increased in amplitude by up to 10% since 1960 in response to rising greenhouse gas concentrations. While this increase may appear modest, it carries significant implications for the frequency and intensity of extreme ENSO events, with potentially widespread climatic and societal consequences.

When considering future projections, a broader consensus emerges. Most climate models predict an increase in ENSO variability throughout the 21^{st} century under transient warming scenarios, driven by changes in the mean climate state such as increased ocean stratification, altered thermocline gradients, and shifts in wind patterns (Geng et al., 2024). However, the extent of projected changes varies greatly among models, reflecting both methodological differences and natural internal variability.

A robust feature across models is the weakening of the Walker circulation and equatorial trade winds under increased greenhouse gas forcing, leading to a reduced zonal SST gradient, a flatter thermocline slope, and basin-wide shoaling of

the thermocline. These ocean-atmosphere adjustments would, in principle, favor stronger ENSO events, yet complex thermodynamic feedbacks and the sensitivity of winds to SST anomalies modulate the actual outcome. Consequently, model projections diverge: some simulations suggest a substantial intensification of ENSO amplitude, while others indicate only minor changes or even a reduction in strength (Hu et al., 2025). Such variability reflects the interplay of competing feedback mechanisms within the coupled ocean-atmosphere system, further compounded by the inherently chaotic and stochastic nature of ENSO, which can mask or amplify the emergence of extreme events (Wang & Picaut, 2004).

Adding to this complexity is the growing recognition that ENSO includes various event types. Observations since the late 1970s show a relative increase in CP El Niño events compared to the traditional EP type. Some studies (e.g., Yeh et al., 2009) suggest that this change in El Niño event type may be related to human-caused climate change, primarily through changes in thermocline structure and zonal wind patterns. However, this interpretation remains debated because of limited observational records and the possibility that internal variability can produce apparent regime shifts over multidecadal timescales. Recent analyses from Coupled Model Intercomparison Project Phase 6 (CMIP6) models have not identified a clear trend in the ratio of CP to EP events (Fredriksen et al., 2020).

In summary, while increasing evidence points to anthropogenic forcing already influencing ENSO variability and event types, significant uncertainties still exist. Differentiating long-term forced trends from natural variability and enhancing the representation of ENSO processes in models remain key challenges. Progress will depend on high-resolution modeling, expanded observational datasets, and targeted analyses of coupled ocean–atmosphere feedbacks, which are crucial for reliable ENSO projections in a warming climate.

1.3 Atlantic Meridional Overturning Circulation (AMOC)

The Atlantic Meridional Overturning Circulation (AMOC) is a key component of the Earth's climate system. It comprises a large-scale system of ocean currents that

redistributes heat and moves saline water masses containing carbon and nutrients across the globe, from the Southern Hemisphere to the Northern Hemisphere and back. It is a branch of the global thermohaline circulation (THC), often called the “global conveyor belt" (Figure 1.3), which is mainly driven by differences in seawater density caused by changes in temperature and salinity.

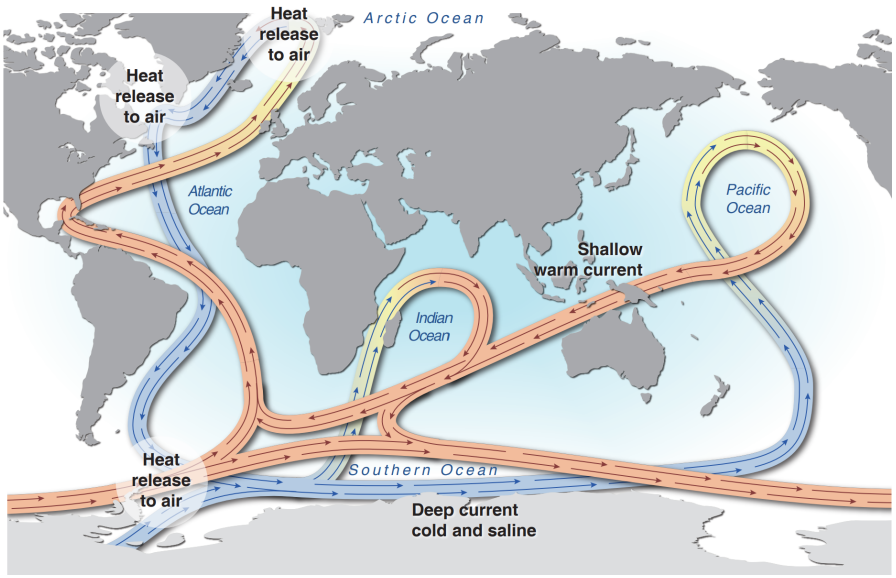

Figure 1.3: Schematic illustration of the global thermohaline circulation. Source: Hugo Ahlenius, UNEP/GRID-Arendal

At its core, the AMOC is maintained by the interaction of surface flows, deep return currents, and smaller-scale eddy processes. These components converge in regions of intense water mass transformation and are driven by both density gradients and atmospheric forcing mechanisms. A simplified overview of the mechanism begins with warm, saline surface waters from the tropical Atlantic flowing northward. As these waters gradually cool and release heat into the atmosphere, they temper the climate of northwestern Europe. This cooling process, combined with increased salinity, mainly from sea ice formation and atmospheric processes, raises the density of the surface waters. Once sufficiently dense, these waters sink in a process known as deep convection, occurring at high latitudes (generally north of 55°N), leading to the formation of the North Atlantic Deep Water (NADW), a crucial component of the overturning circulation. The NADW then flows southward at great depth,

eventually entering the Southern Ocean overturning cell, where approximately 80% of it upwells, facilitated mainly by strong Antarctic winds (Toggweiler & Samuels, 1995). Some of these upwelled waters enter the deep basins of the Indian and Pacific Oceans, while the rest join the upper limb of the overturning circulation, eventually returning to the North Atlantic via surface and intermediate currents. This extensive and complex cycle operates over timescales ranging from centuries to millennia, with a complete overturning of a single parcel of water taking approximately 1,000 years.

The AMOC plays a central role in regulating Earth's climate. It is estimated to transport approximately 0.5 PW of heat annually across equatorial latitudes into the North Atlantic, reaching a peak of nearly 1 PW at 20°N (Buckley & Marshall, 2016). This large-scale heat transport not only connects the hemispheres but also contributes to interhemispheric asymmetries in temperature and precipitation. For instance, the AMOC is considered responsible for making the Northern Hemisphere about 1-2°C warmer than the Southern Hemisphere (Feulner et al., 2013). Additionally, it influences atmospheric circulation patterns, notably displacing the zonal average of the Intertropical Convergence Zone (ITCZ) north of the equator at about 5°N, thereby altering global rainfall distribution (Marshall et al., 2014). Crucially, the AMOC has been identified as one of the tipping elements in the Earth system. The concept of tipping elements refers to large-scale subsystems that can transition into a qualitatively different state once a critical threshold, or tipping point, is crossed. These thresholds, triggered by small perturbations, can lead to disproportionate and potentially irreversible changes in the future behavior of the system (Lenton et al., 2025).

In addition to its role in thermal regulation, the AMOC also plays a pivotal role in the global carbon cycle, enhancing the Atlantic Ocean's capacity as a carbon sink through two principal mechanisms. First, upwelling in the Southern Ocean brings nutrient-rich deep waters to the surface, stimulating phytoplankton growth and thereby increasing marine primary production and photosynthesis. Second, the upwelled water, which has typically been isolated from the atmosphere for around 1000 years, contains lower concentrations of dissolved anthropogenic CO_2, making it more capable of absorbing carbon. Once this water sinks again, it retains the absorbed carbon in the deep ocean, effectively sequestering it and preventing its

return to the atmosphere. Through these processes, the AMOC governs both heat redistribution and deep-ocean carbon uptake, solidifying its role as a key regulator of climate change.

To investigate bi-stability, Stommel (1961) developed an idealized nonlinear two-box model, which simulates the strength of oceanic circulation as a function of density differences driven by both temperature and salinity. Stommel's model revealed that the AMOC could exist in multiple states of equilibrium, including a strong state, similar to today's configuration, as well as a weaker or even reversed state (Weijer et al., 2019). Although it took decades for the climate science community to fully appreciate these findings, Stommel's work gained renewed interest when paleoclimate studies, particularly Greenland ice core records, began to reveal rapid climate shifts in Earth's history. Indeed, paleoclimate reconstructions suggest that the AMOC has undergone significant changes in the past, including substantial weakening or even complete collapse during specific periods of Earth's history. Prominent examples include abrupt climate events such as the Dansgaard-Oeschger oscillations, the Younger Dryas, and various Heinrich events, all of which have been linked to significant disruptions in AMOC dynamics (Lynch-Stieglitz, 2017; Weijer et al., 2019).

More recently, climate models across the full spectrum of complexities have identified the concerning possibility of an AMOC collapse in the future. A central mechanism behind this concern is the salt-advection feedback. Under current conditions, the AMOC maintains itself by transporting saline water into the subpolar North Atlantic, promoting further deep convection. However, if the AMOC weakens, the transport of salt diminishes, reducing convection and further weakening the circulation, creating a positive feedback loop. In extreme cases, this can lead to a state in which no NADW is formed, and the deep Atlantic becomes either stagnant or dominated by upwelling of abyssal waters from Antarctica.

Given that paleoclimate records suggest a real possibility of an AMOC shutdown and considering its potentially severe consequences, scientists have conducted numerous climate model simulations, most notably the so-called "water hosing" experiments. In these simulations, large volumes of freshwater (or anomalies in surface salinity) are artificially added to the North Atlantic or Arctic Oceans to simulate the effects of an AMOC collapse. The results consistently show that a

pronounced weakening of the AMOC would cause substantial cooling across the Northern Hemisphere, only partially balanced by a modest warming in the Southern Hemisphere, particularly in the South Atlantic. The resulting equator-to-pole temperature gradient would intensify mid-latitude westerlies and lead to an eastward extension of the North Atlantic jet stream, thereby enhancing storm activity over Europe. Associated climate impacts would include a reduction in precipitation in the Northern Hemisphere, especially over the Atlantic sector and Europe, alongside increased sea ice cover in the North Atlantic and Nordic Sea, and a southward displacement of the annual mean ITCZ, shifting toward the Southern Hemisphere (Jackson et al., 2015; Zhang & Delworth, 2005).

1.4 Impacts of climate change on AMOC

The AMOC is highly sensitive to climate change due to its dependence on ocean temperature and salinity, both of which are significantly influenced by anthropogenic warming. Rising greenhouse gas concentrations lead to surface ocean warming and increased freshwater input into the North Atlantic, primarily from enhanced precipitation and accelerated melting of Arctic and Greenland ice sheets. These changes reduce surface salinity and increase ocean stratification, especially in the Labrador Sea, where freshwater runoff tends to converge. This increased stratification inhibits vertical mixing by preventing denser, colder water from sinking, thereby weakening the deep convective processes that sustain the lower branch of the AMOC. Additionally, warmer surface waters reduce the meridional (pole-to-equator) temperature gradient, a key thermodynamic driver of heat exchange between ocean and atmosphere. The combined effect of warming and freshening is a reduction in both the density and vertical mixing capacity of the water column, ultimately slowing down the overturning circulation (Brodeau & Koenigk, 2016; Gierz et al., 2015).

Given these physical mechanisms, a critical question arises: is the AMOC already weakening, and if so, to what extent is this decline attributable to current anthropogenic climate change? Direct observations of AMOC strength have only been available since 2004 with the RAPID/MOCHA array at 26.5°N, which has recorded

a decline of 1.0 [0.4-1.6] Sv per decade between 2004 and 2023 (McCarthy et al., 2025). However, due to the short observational record and the system's intrinsic variability, significant uncertainties remain about whether this trend represents a long-term decline or natural decadal fluctuations. While some studies suggest a persistent weakening (e.g., Caesar et al., 2021), others argue that the observed variability does not yet indicate a long-term trend (e.g., Worthington et al., 2021). In light of the observational limitations, climate models offer critical insight into future AMOC behavior. Simulations from state-of-the-art models, including those participating in CMIP6, consistently project a gradual AMOC weakening throughout the 21^{st} century under all Shared Socioeconomic Pathways (Weijer et al., 2020). This scenario is also classified as very likely by the IPCC (2022). While there is general agreement on the direction of change, models diverge considerably in their projections of the rate and magnitude of decline (Bellomo et al., 2021; Weijer et al., 2020). Notably, even under scenarios in which CO_2 concentrations reach four times preindustrial levels, CMIP6 simulations do not generally predict a complete AMOC shutdown (Bellomo et al., 2021). According to the IPCC, a full collapse within this century is considered very unlikely, though it remains a low-probability, high-impact event (IPCC, 2021).

Given these projections, understanding the consequences of even a partial slowdown is crucial. As previously noted, numerous studies have investigated the climatic effects of significant AMOC weakening under preindustrial conditions, particularly through "water hosing" experiments. These studies have provided key insights into the mechanisms and potential patterns of change, offering a valuable framework for assessing AMOC-related risks. However, recent research highlights that such impacts are strongly dependent on the background climate state. In particular, Bellomo and Mehling (2024) conducted targeted model simulations under both preindustrial and strong warming scenarios, finding that while North Atlantic cooling is consistently observed, its intensity and spatial extent differ markedly based on the level of global warming. Their results underscore that the response of key climate variables to AMOC weakening is state-dependent, suggesting that projections based on idealized preindustrial "water hosing" experiments may not be directly applicable to future climate conditions.

1.5 Impacts of AMOC on ENSO

Given AMOC's potential role on global climate change and its potential tipping as well as the role of ENSO as the leading mode of internal climate variability, it is of growing concern to investigate the role of AMOC weakening on ENSO variability. Understanding this linkage is also critical for explaining part of the observed climate variability and for improving the predictive skill of coupled climate models.

It is well known that climatic consequences of a weakened AMOC are not confined to the Atlantic basin, but specific impacts are still debated. Most climate models agree on robust global-scale responses to an AMOC shutdown, including a widespread Northern Hemisphere cooling. This cooling increases the interhemispheric temperature gradient, which in turn perturbs the meridional energy balance. As a consequence, the ITCZ shifts southward and the northern Hadley cell intensifies. These large-scale adjustments in the coupled ocean–atmosphere system constitute the background for potential teleconnections with the tropical Pacific. Among the most significant of these remote impacts is the modulation of ENSO variability.

Although the potential importance of this teleconnection is widely recognized, systematic research on AMOC-ENSO link is relatively recent and still limited in scope. To date, there is no consensus regarding either the magnitude or even the sign of ENSO's response to AMOC changes (Hu et al., 2025). The most frequently proposed mechanism involves atmospheric teleconnections: cooling in the North Atlantic combined with warming in the South Atlantic shifts the ITCZ southward, modifies cross-equatorial winds, and alters the Walker circulation. These changes can propagate into the Pacific, where they influence trade winds and convection, thereby modifying the mean state of the equatorial Pacific and affecting ENSO variability through coupled air-sea feedbacks.

Seminal works by Dong and Sutton (2007) and Timmermann et al. (2007), which use coupled climate models forced with freshwater perturbations to mimic an AMOC shutdown, illustrate this mechanism. Both studies showed that a weakened AMOC produces meridionally asymmetric changes in the tropical Pacific mean state, notably a reduction in the seasonal SST cycle and anomalous cross-equatorial winds. These adjustments favored stronger ENSO variability. In HadCM3, analyzed

by Dong and Sutton, El Niño events intensified and shifted eastward. Timmermann and colleagues, analyzing multiple CMIP3 models, found similar behavior across most of them. They proposed the so-called nonlinear frequency entrainment mechanism: a weaker seasonal cycle in the eastern Pacific facilitates stronger ENSO excursions. In essence, ENSO behaves as a nonlinear oscillator whose intrinsic frequency interacts with the annual cycle. When the seasonal forcing weakens, ENSO is less constrained by phase-locking and can produce larger amplitude events. However, they assert that this mechanism strongly depends on the existing background conditions and, in particular, on the simulated thermocline depth anomalies.
More recent studies have challenged this interpretation. Williamson et al. (2018), using a higher-resolution version of the same model employed by Dong and Sutton, confirmed mean-state changes such as central Pacific warming, weakened trade winds, and a reduced seasonal cycle. However, instead of enhanced ENSO amplitude, they observed an eastward shift in variability without a significant change in magnitude. They argued that the growth mechanisms were counteracted by reduced stochastic forcing from the atmosphere, producing a neutral effect on variance. This result emphasized the importance of atmospheric noise and stochastic feedback in shaping the ENSO response to remote forcings.
In constrast, Orihuela-Pinto et al. (2022) offered a totally different mechanism. They found that ENSO variability decreased by about 30% following an AMOC collapse. In their simulations, the AMOC shutdown produced a cooler tropical Pacific and a stronger Walker circulation. These conditions weakened air–sea coupling by reducing the efficiency of surface winds in driving thermocline adjustments, partly due to a deepened mixed layer. As a result, the growth of ENSO events was damped, and extreme El Niño events became markedly rarer. This mechanism differs sharply from the nonlinear frequency entrainment hypothesis, instead attributing the reduction in ENSO variability to a weakening of the Bjerknes feedback.
Taken together, these divergent findings underscore the complexity of AMOC-ENSO interactions. These discrepancies reveal a strong model dependence, highlighting how different balances of amplifying and damping feedbacks emerge across climate models and background states. Additional evidence from Molina et al. (2022) further suggests that the ENSO response to AMOC weakening may also depend

on the timescale of the perturbation. In their extended simulations using the same climate model as Orihuela-Pinto et al., a more extended AMOC shutdown produced an increased ENSO amplitude despite the initial damping response, implying that the balance between feedbacks evolves over time even within a single model framework.

The challenge grows further in the context of anthropogenic climate change. Many early water hosing experiments simulated abrupt AMOC shutdowns, more relevant to paleoclimate than to the gradual weakening projected for the 21^{st} century. Addressing this gap, Liu et al. (2023) analyzed AMOC-ENSO interactions under future climate scenarios characterized by progressive greenhouse forcing without a complete AMOC shutdown. Their simulations show that a relatively weaker AMOC leads to a reduction in the amplitude of the equatorial Pacific SST annual cycle. At the same time, it slightly enhances ENSO variance by approximately 11%, thereby partially counteracting the modest reduction in ENSO variability induced by global warming. However, these effects remain small with respect to internal climate variability. According to their analysis of the Bjerknes stability index, the modest intensification of ENSO activity arises from an enhanced Ekman upwelling feedback, manifested as stronger atmospheric responses to SST anomalies and amplified oceanic upwelling driven by wind stress perturbations.

In summary, previous research shows that several mechanisms compete with varying influence across models, leading to diverse outcomes. What is clear is that an AMOC weakening can trigger large-scale atmospheric teleconnections that reach the tropical Pacific, but the impacts on ENSO variability are still not fully understood. Clarifying this relationship will require coordinated multi-model efforts and the integration of paleoclimate and observational data. Advancing this research is crucial for understanding how these two key systems may co-evolve under future climate change.

Chapter 2

Motivation

The introduction highlighted the growing body of evidence that the AMOC and ENSO are not independent phenomena but can be connected by complex atmospheric and oceanic teleconnections. Multiple physical processes interact, while the literature remains inconclusive. Some studies report amplified ENSO variability under AMOC weakening, others find damped variability, while still others suggest little or no change. This lack of consensus reflects the multiplicity of competing feedbacks involved and the strong sensitivity of outcomes to model formulation and to the background climate state.

A further complication arises from the fact that most modeling studies addressing AMOC-ENSO interactions have been conducted under preindustrial-like conditions, often using idealized freshwater-hosing experiments. Those experiments have been valuable in revealing the governing mechanisms and possible teleconnection pathways, but they do not fully address how such mechanisms operate in the context of a warming climate. In other words, while preindustrial experiments probe what a significant, abrupt AMOC perturbation can do, they do not capture how the CO_2-driven AMOC decline expected over the 21^{st} century may influence ENSO under anthropogenic warming.

This thesis aims to address this gap by investigating the impacts of AMOC weakening on ENSO in two contrasting climate states: a preindustrial world and a greenhouse-warmed climate. By explicitly comparing these backgrounds, the study

aims to clarify the role of state dependence in shaping the AMOC-ENSO teleconnection and to provide new insights into how these two key components of the climate system may interact under future climate change. This approach makes it possible to disentangle the specific influence of AMOC weakening from the broader effects of greenhouse forcing, thereby reducing uncertainties surrounding future ENSO projections.

Chapter 3

Datasets and models

The analysis is based on simulations performed with the EC-Earth3 model, a state-of-the-art coupled general circulation model that participates in CMIP6. Two climate backgrounds are considered: a preindustrial control and a 4xCO_2 experiment, in which atmospheric CO_2 concentrations are quadrupled relative to preindustrial levels. The latter configuration is broadly representative of conditions projected to occur by the end of the 21^{st} century under the SSP5-8.5 scenario. Within each background, two contrasting states are analyzed: one with a strong AMOC and one with a weak AMOC, resulting in four targeted simulations in total. This design enables a direct comparison of AMOC impacts across climate states. Before focusing on AMOC–ENSO interactions, the fidelity of EC-Earth3 in simulating ENSO was first assessed. Model outputs were evaluated against two observational datasets to ensure that the model reproduces the fundamental characteristics of ENSO variability and thus provides a credible basis for the subsequent analysis.

3.1 Observations

To evaluate the performance of the climate model in characterizing ENSO dynamics, three observational datasets were employed, focusing on variables central to tropical Pacific variability: SST, precipitation, surface winds, and thermocline depth.
SST was taken from two widely used datasets. The first is ERSSTv5 (Extended

Reconstructed Sea Surface Temperature, version 5) (Huang et al., 2017), developed by NOAA. It provides global monthly fields from 1870 to 2024 on a regular 2°×2° grid, and it is constructed from ship, buoy, and satellite observations combined with statistical reconstruction methods to fill spatial and temporal gaps. The second is HadISST (Hadley Centre Sea Ice and Sea Surface Temperature) (Rayner et al., 2003), produced by the UK Met Office Hadley Centre. It spans the same temporal coverage but at a finer 1°×1° grid, using optimal interpolation techniques to merge in situ and satellite observations, and also provides sea-ice concentration.
Precipitation data were obtained from the ERA5 reanalysis (Hersbach et al., 2020), developed by ECMWF. It provides global monthly fields from 1940 to 2024 at a 0.25°×0.25° resolution. The raw variable tp, obtained directly from the dataset, was converted into monthly precipitation rates in mm/day.
Surface wind fields were also taken from ERA5, using the 10-metre wind components u10 and v10, available monthly from 1940 to 2024 on the same 0.25° grid.
Finally, the thermocline depth was represented by the depth of the 20°C isotherm Z20, also derived from ERA5 for the period 1958-2024 at 0.25° resolution. Z20 is a standard proxy for thermocline depth and is widely used in ENSO diagnostics.
All datasets underwent detrending prior to analysis. At each grid point, a linear least-squares regression against time was applied to remove long-term trends. This step isolates internal climate variability, particularly the interannual fluctuations relevant to ENSO, from externally forced changes such as anthropogenic warming.

3.2 EC-Earth3

Climate models provide the essential framework for investigating past, present, and future climate variability. They represent the climate system through numerical solutions of the governing physical equations for mass, momentum, and energy. By discretizing the Earth into three-dimensional grid cells, these models resolve exchanges of heat, moisture, and momentum across the atmosphere, ocean, land, and cryosphere (NOAA, 2014).
The experiments in this study were conducted with EC-Earth3, a state-of-the-art coupled general circulation model (GCM) developed by a consortium of European

research institutions and contributing to the CMIP6 archive (Döscher et al., 2022). As a fully coupled Earth system model, EC-Earth3 integrates the major components of the climate system, including the atmosphere, ocean, land surface, and sea ice, allowing for two-way interactions among them. The coupling process is highly complicated, as the codes for the different components are developed independently and may differ in both spatial and temporal resolution. This integration is nevertheless essential for investigating processes like the AMOC–ENSO teleconnection, which emerge from feedbacks across different subsystems. Specifically, EC-Earth3 couples the ECMWF IFS cy36r4 atmospheric model, the land-surface scheme H-TESSEL, the NEMO 3.6 ocean model, and the LIM3 sea-ice component. These are linked through the OASIS3-MCT coupler, which exchanges fluxes among the different components. The atmospheric resolution is TL255L91 ($\sim$80 km horizontal resolution with 91 vertical levels), while the ocean uses ORCA1L75 ($\sim$100 km horizontal resolution with 75 vertical levels). These standard CMIP6 resolutions provide a balance between computational efficiency and the ability to represent large-scale climate processes.

Despite their sophistication, climate models still face persistent challenges in simulating ENSO. Coupled GCMs remain the most reliable framework because they simulate multi-scale processes interactively across the atmosphere and ocean basins, but long-standing mean-state biases limit their skill. In particular, tropical Pacific biases reduce the model's ability to capture ENSO diversity, and even state-of-the-art systems struggle to reproduce the observed ENSO power spectrum, including its dominant spectral peaks (Wang et al., 2025). Progress in ENSO modeling requires ongoing efforts in several areas:

- Advancing the theoretical understanding of ENSO dynamics and their modification under anthropogenic forcing;

- Expanding reconstructions of SST and precipitation using multi-proxy datasets with higher spatial and temporal coverage;

- Reducing systematic model biases by integrating physical theory with observational constraints and improving the representation of unresolved processes and coupled feedbacks (Alizadeh, 2022).

Models' limitations must be considered when interpreting results from model-based ENSO studies. Nevertheless, coupled ocean–atmosphere models have significantly improved in recent decades, achieving sufficient realism to explore questions beyond the reach of the relatively short observational record (Deser et al., 2012).

3.3 Experimental design

The experimental framework combines two background climate states (preindustrial and $4\times CO_2$) with two AMOC configurations (strong and weak), resulting in four targeted simulations. This design allows for a systematic investigation of how AMOC strength modulates ENSO under contrasting climate conditions.

The preindustrial simulations are documented in Bellomo et al. (2023). A 500-year preindustrial control simulation is performed with radiative forcing fixed at 1850 levels ($\sim$284 ppm CO_2), such that all variability is internally generated. This control simulation is compared with a water hosing experiment, in which a freshwater anomaly of 0.3 Sv is uniformly applied north of 50°N in the Atlantic and Arctic Oceans for 140 years. Afterward, the anomaly is removed, and the model evolves freely for an additional 70 years, resulting in a total integration length of 210 years. For clarity, these two experiments will hereafter be referred to as "Strong AMOC under preindustrial climate" (Preindustrial control) and "Weak AMOC under preindustrial climate" (Water hosing), respectively.

For the greenhouse-warming case, the abrupt $4\times CO_2$ experiment is initialized from the preindustrial control and forced with a fixed CO_2 concentration equal to four times preindustrial levels for 150 years. This concentration is comparable to that projected under the SSP5-8.5 (Shared Socioeconomic Pathway 5) high-emission scenario, which represents a fossil fuel-intensive future with limited development of renewable energy and no implementation of climate mitigation policies (O'Neill et al., 2016). The strong radiative forcing associated with this experiment induces both pronounced global warming and a substantial weakening of the AMOC. To isolate the role of AMOC strength under greenhouse forcing, a fixed-AMOC experiment is conducted. This simulation is initialized from the abrupt $4\times CO_2$ state but applies a positive salinity flux of 0.6 Sv poleward of 50°N in the Atlantic and

Arctic Oceans. This artificial forcing counteracts the weakening of the AMOC induced by CO_2, maintaining the overturning circulation closer to preindustrial levels. For clarity, these two experiments will hereafter be referred to as "Weak AMOC under 4×CO_2 climate" (Abrupt 4×CO_2) and "Strong AMOC under 4×CO_2 climate" (Fixed AMOC), respectively.
In all virtual salinity flux experiments, global ocean salinity is conserved by applying compensating corrections elsewhere, thereby ensuring volume conservation. A summary of all experiments is provided in Table 1.

Experiment name	**Reference name**	**Duration [years]**	**Description**
Preindustrial control	Strong AMOC in preindustrial climate	500	Preindustrial forcing (fixed at 1850 values). All variability is internal.
Water hosing	Weak AMOC in preindustrial climate	210	Freshwater anomaly of 0.3 Sv north of 50°N applied for 140 years, followed by 70 years of free evolution.
Abrupt 4xCO_2	Weak AMOC in 4xCO_2 climate	150	Initialized from picontrol, forced with quadrupled CO_2 concentration fixed at 4× preindustrial.
Fixed AMOC	Strong AMOC in 4xCO_2 climate	150	Initialized from abrupt 4×CO_2. Positive salinity flux is applied to maintain AMOC strength. Results reported as the ensemble mean of three members.

Table 3.1: Description of the experimental design.

The behavior of the AMOC in the four experiments is evaluated using the AMOC index, defined as the annual mean maximum of the meridional overturning streamfunction at 26.5°N between 500 and 2000 m depth.

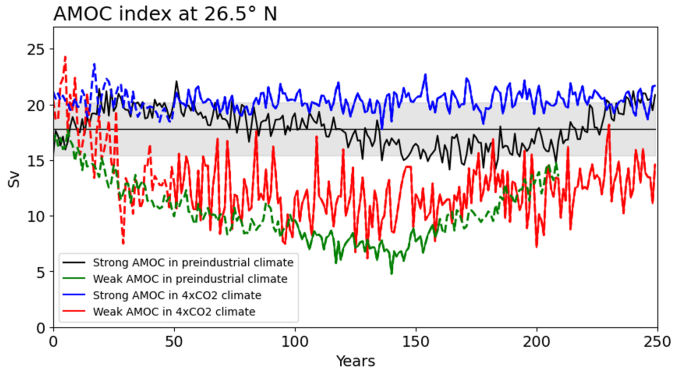

Figure 3.1: AMOC index time series at 26.5°N for the EC-Earth3 experiments.

Figure 3.1 shows the time series of the AMOC index across the experiments. The Strong AMOC in preindustrial climate experiment is also represented by its long-term mean over the 500-year integration (thick black line), while the gray shading denotes ±1.5 standard deviations, providing an estimate of internal variability. Solid and dashed segments in the other three experiments distinguish the periods included in the following analyses from those excluded. In detail, for the Weak AMOC in preindustrial climate, only the 60-year interval (model years 100-159) in which AMOC strength falls below half of the preindustrial mean was retained. In the $4\times CO_2$ experiments, the first 50 years are omitted to exclude the transient adjustment following the abrupt quadrupling of CO_2 concentration and, in the fixed-AMOC case, the imposition of the salinity flux.
In the preindustrial simulations, the AMOC exhibits a mean strength of 17.8 ± 2.4 Sv for the strong-AMOC case and 7.61 Sv for the weak-AMOC case, corresponding to a 57.3% reduction. Under $4\times CO_2$ forcing, the strong-AMOC experiment maintains an average of 20.32 Sv, while the weak-AMOC configuration stabilizes at 12.03 Sv, reflecting a 40.8% reduction relative to its strong-AMOC counterpart. Analyzing the details of each experiment curve, in the preindustrial climate, the Strong AMOC remains relatively stable, with natural variability confined to a range of approximately 3 Sv, indicating a system in near-equilibrium. When freshwater forcing is applied, the circulation undergoes the most substantial decline among all scenarios, reaching minimum values of 6-7 Sv. Unlike the corresponding $4\times CO_2$ case, however, the AMOC gradually recovers during the final phase of the simulation, approaching intermediate values between its maximum and minimum

states. In the Strong AMOC in 4×CO_2 climate, the imposed positive salinity flux successfully counteracts the weakening induced by greenhouse forcing, resulting in AMOC values that remain well within the envelope of internal variability estimated from the control run. The circulation exhibits interannual fluctuations but no discernible long-term trend. In contrast, the weak AMOC experiences a steep decline in the first 50 years, then stabilizes at lower levels without signs of recovery. Another way to investigate the behavior of the AMOC across the four experiments is through the analysis of the ocean meridional mass streamfunction in the Atlantic-Arctic region, shown in Figure 3.2. The streamfunction is averaged over the selected analysis period for each simulation, corresponding to the continuous segments in Figure 3.1. To better compare the experiments, Figure 3.3 illustrates the streamfunction differences between the various configurations.

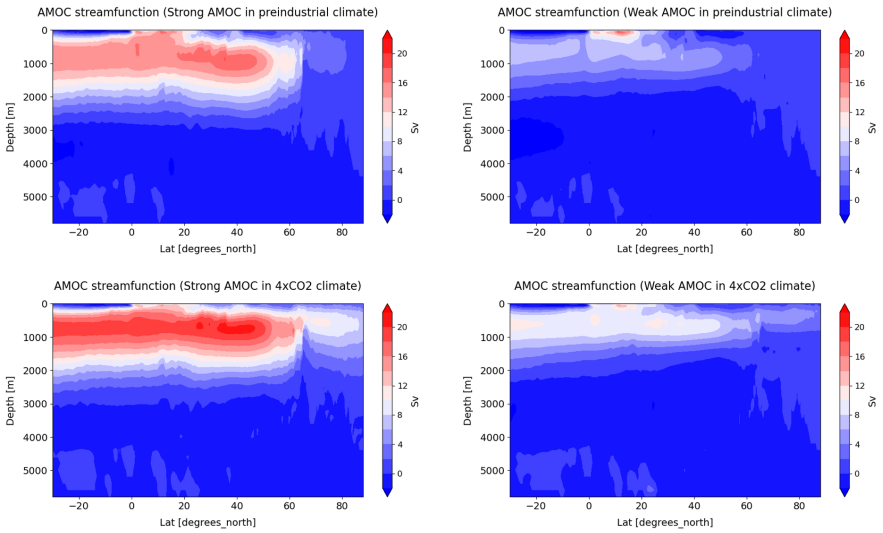

Figure 3.2: AMOC streamfunctions across the four experiments.

As expected, the overturning cell is substantially weaker in the Weak AMOC cases relative to their Strong AMOC counterparts, both under preindustrial and 4xCO_2 conditions. In both difference plots (Figures 3.3a and 3.3b), the most significant reduction occurs at latitudes between 40°N and 60°N. However, under a 4xCO_2 climate, a considerable weakening also emerges at polar latitudes, a feature that is absent, or at least much less pronounced, in the preindustrial case. In fact,

Figure 3.2 shows that in the strong AMOC simulation under $4\times CO_2$ forcing, the imposed salinity flux not only compensates for the CO_2-induced weakening but also enhances the circulation north of 60°N, producing a distinct northward extension of the AMOC cell.

Another robust feature is that both $4\times CO_2$ experiments display an overall stronger overturning cell compared to their preindustrial analogues (Figure 3.2). Moreover, Figure 3.3c highlights that, without any external perturbations designed to artificially enhance or suppress the circulation, quadrupling CO_2 indeed results in a weakening of the AMOC, consistent with what has been repeatedly emphasized in the introduction. While a reduction in strength is expected, a complete shutdown does not occur, even under the most extreme forcing scenario, such as a $4\times CO_2$ increase. As previously discussed, the SSP5-8.5 scenario represents the "worst-case" projection, further confirming the very low likelihood of a total collapse occurring within the current century. Nevertheless, the projected reductions in AMOC intensity remain highly significant.

Taken together, the streamfunction patterns confirm that both the strength and spatial structure of the AMOC are susceptible to background climate state as well as to imposed freshwater or salinity perturbations.

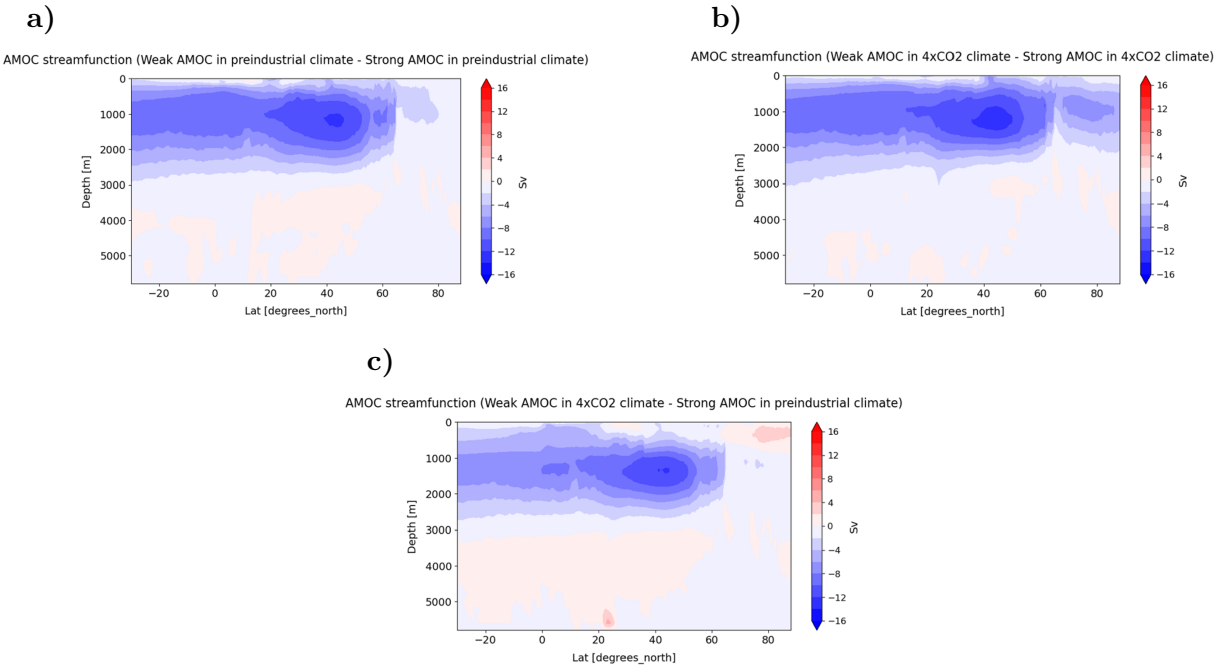

Figure 3.3: AMOC streamfunction differences across experiments.

Chapter 4

Methodology

This study investigates the mechanisms and characteristics of ENSO variability under different climatic background states and AMOC strengths. To this end, a comprehensive methodological framework was developed, combining observational datasets with climate model simulations. The approach integrates diagnostic analyses that quantify ENSO amplitude, frequency, persistence, and spatial evolution, ensuring a consistent comparison across experiments.

The analysis proceeds in several stages. First, all datasets were preprocessed to ensure temporal and spatial consistency. Subsequently, SST anomalies were computed relative to the monthly climatology to isolate interannual variability, the key timescale of ENSO dynamics. The Niño 3.4 index was then derived from area-averaged SST anomalies in the central–eastern tropical Pacific and adopted as the primary diagnostic variable for quantifying ENSO variability. Subsequently, a set of statistical analyses was performed to characterize the amplitude and temporal behavior of ENSO. These included the computation of standard deviations, power spectral densities, and autocorrelation functions to assess the strength, dominant periodicities, and persistence of ENSO-related anomalies. Finally, ENSO events were objectively identified based on the Niño 3.4 index, and composite analyses were constructed for key oceanic and atmospheric variables.

Collectively, this methodology offers a solid framework to examine how variations in AMOC strength and background climate conditions influence ENSO behavior, both in terms of variability and event structure. Each of these methodological

steps is explained in detail in the following sections.

4.1 Data processing

All data processing, analysis, and visualization were performed using the Python programming language, supported by a suite of specialized scientific libraries for data management, statistical computation, and geospatial representation. Among these, Xarray was primarily employed to handle multidimensional labeled datasets stored in NetCDF format, the standard structure for storing climate and oceanographic data, enabling efficient manipulation, aggregation, and analysis of large spatiotemporal fields.

Prior to analysis, all SST datasets, both observational and model-based, underwent a consistent preprocessing procedure to ensure temporal and spatial consistency. The observational datasets (ERSSTv5 and HadISST) were restricted to their common temporal window (1870-2024), maximizing the overlapping time span between products. In contrast, model SST data, derived from the preindustrial control simulation, were analyzed over their whole 500-year integration period to capture the system's intrinsic variability.

To establish a coherent temporal framework, time coordinates were standardized across all datasets. Spatial regridding and interpolation were applied where necessary to harmonize resolutions and allow direct gridpoint-to-gridpoint comparisons between modeled and observed fields. To isolate internal climate variability and remove externally forced long-term trends, each gridpoint SST time series from the observational datasets was linearly detrended according to:

$$T^*(i,j,t) = T(i,j,t) - \Big[\alpha_{i,j} + \beta_{i,j}\, t\Big] \tag{4.1}$$

where $\alpha_{(i,j)}$ and $\beta_{(i,j)}$ represent the intercept and slope of the least-squares linear regression over time, respectively. This detrending procedure removes the secular warming signal present in observational records, thereby ensuring direct comparability with the preindustrial control simulation, which is inherently free from anthropogenic forcing. As a result, all subsequent analyses focus solely on internal modes of climate variability.

4.2 SST anomalies

SST anomalies constitute the fundamental variable in all analyses of this study, serving as the basis for the metrics employed to characterize ENSO variability. In climate science, SST anomalies quantify the deviations of sea surface temperatures from their long-term mean state, thereby indicating how oceanic surface conditions differ from their climatological baseline. They are vital for detecting and evaluating phenomena such as El Niño and La Niña, which are inherently characterized by sustained positive or negative SST departures in the equatorial Pacific.
In this work, SST anomalies were computed relative to the monthly climatology, i.e., the long-term average SST for each calendar month, to remove the influence of the seasonal cycle:

$$T'(i,j,t) = T(i,j,t) - \overline{T}_m(i,j) \tag{4.2}$$

where $T(i,j,t)$ denotes the SST field at spatial coordinates i, j and time t (detrended in the case of observational datasets) and $\overline{T}_m(i,j)$ represents the climatological mean for month m at the same grid point. This formulation filters out the mean seasonal signal, isolating interannual variability, the dominant timescale on which ENSO operates. Since ENSO events typically develop over several months and reach their peak during the boreal winter, removing the regular annual cycle is essential to avoid aliasing intrinsic ENSO variability with the recurring seasonal fluctuations.

4.3 Niño 3.4 index

To quantitatively monitor variability in the tropical Pacific, several indices have been developed, each based on area-averaged SST anomalies over specific regions. Among these, the Niño 3.4 index is the most widely used benchmark for identifying and analyzing El Niño and La Niña events. It was introduced in 1996 by the Climate Prediction Center of NOAA's National Centers for Environmental Prediction (Trenberth, 1997). The nomenclature "3.4" originates from the historical numbering of equatorial Pacific regions along early ship routes. The Niño 3.4 region extends from 5°S-5°N and 170°W-120°W, encompassing the central-eastern equatorial Pacific (Figure 4.1). The index is calculated as the area-weighted mean of monthly

SST anomalies within this domain.
This index is adopted as the primary diagnostic for ENSO monitoring because it effectively captures basin-scale variability, representing both Eastern and Central Pacific ENSO types (Trenberth, 1997). Situated along the western margin of the equatorial cold tongue, it sensitively reflects fluctuations in SST gradients that are closely tied to variations in deep tropical convection and atmospheric circulation.

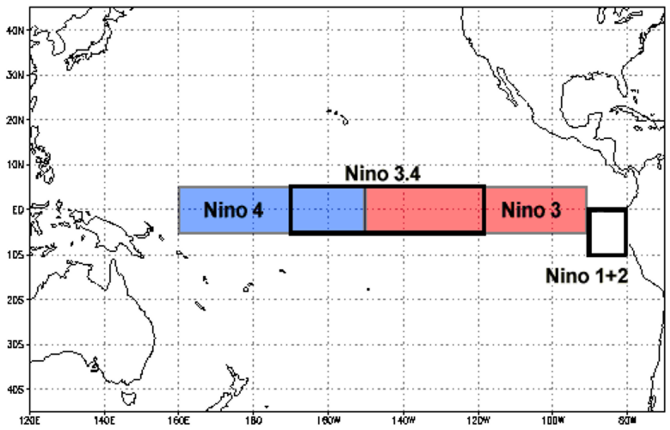

Figure 4.1: Spatial extent of the Niño 3.4 region.

4.4 ENSO amplitude and temporal characteristics

ENSO variability was quantified through a series of statistical metrics designed to characterize both its amplitude and temporal behavior.
The first diagnostic involved calculating the standard deviation of SST anomalies at each grid point within the tropical Indo-Pacific domain. This measure captures the intensity of local SST fluctuations relative to their mean state, thereby mapping the spatial distribution and magnitude of variability throughout the basin. The standard deviation at each grid point (i, j) was computed as:

$$\sigma_T(i,j) = \sqrt{\frac{1}{N-1}\sum_{t=1}^{N}\left[T'(i,j,t) - \overline{T}'(i,j)\right]^2} \tag{4.3}$$

where $T'(i,j,t)$ denotes the SST anomaly at time t, and $\overline{T}'(i,j)$ represents its temporal mean. This formulation highlights regions of maximum SST variability associated with ENSO and other tropical modes, typically concentrated in the central-eastern equatorial Pacific.

Building upon this spatial characterization, the standard deviation of the Niño 3.4 index was subsequently employed as a representative measure of ENSO amplitude. This index offers an integrated metric of SST fluctuations within the central–eastern equatorial Pacific and functions as the primary quantitative indicator of ENSO strength. To examine the seasonal modulation of ENSO variability, the standard deviation of monthly Niño 3.4 anomalies was calculated for each calendar month, resulting in a 12-month cycle that delineates the evolution of ENSO amplitude throughout the year and verifies its characteristic phase-locking to the boreal winter, a period during which SST anomalies generally attain their peak intensity.

Low-frequency modulation of ENSO amplitude was evaluated by applying a 30-year running standard deviation to the monthly Niño-3.4 index, quantifying multidecadal variability in ENSO strength:

$$\sigma_{30\mathrm{y}}(t) = \sqrt{\frac{1}{n-1}\sum_{k=t-15}^{t+15}\Big[\text{Niño 3.4}(k) - \overline{\text{Niño 3.4}}_{30\mathrm{y}}(t)\Big]^2} \tag{4.4}$$

This method highlights slow modulation of ENSO amplitude, providing an indicator of changes in the intensity of El Niño and La Niña events over time.

To identify the dominant periodicities and the distribution of variance across frequency bands, the power spectral density (PSD) of the Niño 3.4 SST index was computed using the Welch method. This approach reduces spectral variance by dividing the time series into overlapping segments, applying a tapering window, and averaging their individual periodograms:

$$P(f) = \frac{1}{K}\sum_{k=1}^{K}\frac{1}{N}\Big|\mathrm{FFT}\Big\{w(n)\,x_k(n)\Big\}\Big|^2 \tag{4.5}$$

where $x_k(n)$ represents the k-th data segment of length N, $w(n)$ is a tapering (Hann) window, K is the number of overlapping segments averaged and FFT is the Fast Fourier Transform. This method provides a smoother and statistically

more robust estimate of spectral power than a single Fourier transform. To assess spectral uncertainty in the model simulations, the full integration was divided into consecutive 100-year segments. A spectrum was computed for each segment, and their inter-segment standard deviation $\sigma_P(f)$ was used to estimate the 95% confidence interval around the mean model spectrum:

$$\mathrm{CI}_{95\%}(f) = P(f) \pm 1.96 \, \frac{\sigma_P(f)}{\sqrt{N_s}} \tag{4.6}$$

where N_s is the number of segments. This provides a robust measure of internal variability in the simulated ENSO spectral power, distinguishing persistent periodic components from stochastic noise.

Finally, the temporal persistence of ENSO-related SST anomalies was assessed through autocorrelation analysis of the Niño 3.4 index. Autocorrelation measures the similarity between a time series and a lagged version of itself, offering insight into the system's memory. Prior to computation, a three-point binomial filter was applied to suppress high-frequency noise and emphasize the interannual signal:

$$T_s(t_i) = \frac{1}{4}\Big[T(t_{i-1}) + 2\,T(t_i) + T(t_{i+1})\Big] \tag{4.7}$$

Autocorrelations were then calculated with respect to December anomalies, the canonical ENSO peak phase, over lags of ± 5 years:

$$r(\tau) = \frac{\mathrm{cov}\left[N_{3.4}^{\mathrm{Dec}}(t),\, N_{3.4}(t+\tau)\right]}{\sigma_{N_{3.4}^{\mathrm{Dec}}}\, \sigma_{N_{3.4}(t+\tau)}} \tag{4.8}$$

where τ denotes the lag in months. This formulation reveals the persistence and recurrence patterns in ENSO evolution, such as whether warm anomalies in a given December tend to persist, decay, or reverse in subsequent years.

4.5 Identification of ENSO events and composite analysis

The identification of ENSO events and the construction of composites constitute essential methodological steps for investigating the spatial and temporal evolution of SST anomalies and their coupled ocean-atmosphere responses.

There is no universally accepted criterion for defining the beginning or end of an El Niño or La Niña event, as these phenomena arise from complex interactions between oceanic and atmospheric anomalies rather than the exceedance of a fixed threshold. Following the definition provided by NOAA's Climate Prediction Center, an El Niño (La Niña) event is identified when the 3-month running mean of SST anomalies in the Niño 3.4 region remains above 0.5°C (below -0.5°C) for at least five consecutive overlapping seasons. This operational definition captures sustained oceanic warm (or cold) phases, although a physically consistent classification also requires concomitant atmospheric anomalies, notably enhanced (suppressed) convection near the dateline and westerly (easterly) surface wind anomalies across the central Pacific.

Following Okumura & Deser (2010), ENSO events were objectively detected in this study using the smoothed Niño 3.4 index. The raw index was filtered with a three-point binomial filter to suppress high-frequency noise and isolate interannual variability. December values of the filtered series, corresponding to the canonical ENSO peak phase, were used to define event years according to:

$$\text{El Niño: } N_{3.4}^{\text{Dec}}(t) > \sigma_{\text{Dec}}$$

$$\text{La Niña: } N_{3.4}^{\text{Dec}}(t) < -\sigma_{\text{Dec}}$$

where $N_{3.4}^{\text{Dec}}(t)$ denotes the smoothed December Niño 3.4 index for year t and σ_{Dec} its standard deviation computed over all December values in the record. Borderline cases were verified through manual inspection and comparison with historical ENSO chronologies to ensure physical consistency. Following Trenberth (1997), events characterized by two consecutive years with warm or cold anomalies (e.g., 1940/41, 1949/50, 1986/87, and 1998/99) were regarded as single episodes.

Once El Niño and La Niña years were identified, a composite analysis was performed

to extract the mean spatio-temporal evolution of SST anomalies associated with each ENSO phase. SST data were first restricted to the equatorial band (4°S-4°N, 120°E-80°W) and then meridionally averaged to produce longitude–time sections. For each event, monthly SST anomalies were extracted over a three-year window centered on the ENSO peak (January of year 0 to May of year +2) and then averaged across all identified events.

To capture the atmosphere-ocean evolution through the different stages of ENSO, seasonal composites were constructed for SST, precipitation, surface wind, and thermocline depth anomalies across eight consecutive seasonal phases from the development year (year 0) to two years after onset (year +2). Each composite season was defined as the mean of the corresponding three-month anomalies. Seasonal means were then averaged across all selected El Niño events to produce the final composite.

Chapter 5

Results

5.1 Assessment of EC-Earth3 against observations

This section evaluates the ability of the EC-Earth3 climate model to reproduce the main characteristics of ENSO under preindustrial conditions. Despite substantial progress in the representation of ENSO within coupled atmosphere–ocean general circulation models, notable challenges persist. However, observational records, being relatively short, are insufficient to capture the full spectrum of natural ENSO variability, making climate models indispensable tools for investigating its dynamics. Previous studies have emphasized the limitations of relying solely on observations to assess the ENSO-forced response (Deser et al., 2017; Stevenson et al., 2010), highlighting that much of the apparent uncertainty arises from internal atmospheric variability. Stevenson et al. (2010) further demonstrated that a record length of at least 250 years is required to evaluate changes in ENSO with 90% confidence, underscoring the importance of long-term simulations.

This study employs the Strong AMOC in preindustrial climate experiment, consisting of a 500-year control integration under constant 1850 atmospheric CO_2 concentrations, providing a statistically robust basis for the characterization of ENSO variability. Model performance is assessed by comparing it with two detrended observational datasets, focusing primarily on SST and selected oceanic and atmospheric variables that describe coupled ocean–atmosphere feedbacks.

5.1.1 Niño-3.4 SST variability

The representation of tropical Indo-Pacific SST variability offers a comprehensive test of EC-Earth3's skill in simulating the processes underlying ENSO. At the basin scale, the model reproduces the climatological annual mean SST distribution with remarkable fidelity (Figure 5.1). The equatorial Pacific cold tongue is well captured in both its zonal extent and meridional position, extending from the South American coast into the central Pacific, in agreement with observations. Meridional SST gradients across the equator and the temperature contrast between the western Pacific warm pool and the eastern cold tongue are realistically simulated, indicating a credible representation of the mean ocean circulation and surface heat fluxes. However, minor discrepancies persist, notably a slightly warmer and more extensive western Pacific warm pool. The 29°C isotherm, absent in ERSSTv5 and confined to a smaller area in HadISST, covers a broader region in EC-Earth3, indicating a modest warm bias in the model mean state.
The spatial pattern of SST anomalies variability further confirms the model's realism (Figure 5.1). EC-Earth3 reproduces the observed centers of interannual variability along the equatorial Pacific, with maximum standard deviations located over the cold tongue region and secondary peaks in the North Pacific midlatitudes. The amplitude and spatial distribution of variability broadly align with both ERSSTv5 and HadISST, confirming that the model captures the leading modes of Indo-Pacific SST fluctuations. Some regional differences remain, including a westward displacement of the maximum variability and a mild underestimation of its intensity in the equatorial belt. At higher northern latitudes, discrepancies are larger, reflecting different treatments of sea-ice variability across datasets, though these have limited relevance for the present ENSO-focused analysis.

When differences between the model and the two observational products are explicitly examined (Figure 5.2), they remain generally small: mean-state SST deviations remain mostly within ±2°C, with EC-Earth3 being slightly colder in the central equatorial Pacific and warmer along the South American coast. For SST variability, differences relative to ERSSTv5 rarely exceed ±0.25°C, while slightly larger deviations appear with HadISST, especially at higher latitudes. collectively, these results demonstrate that EC-Earth3 reproduces both the spatial structure and magnitude of observed interannual variability with credible accuracy.

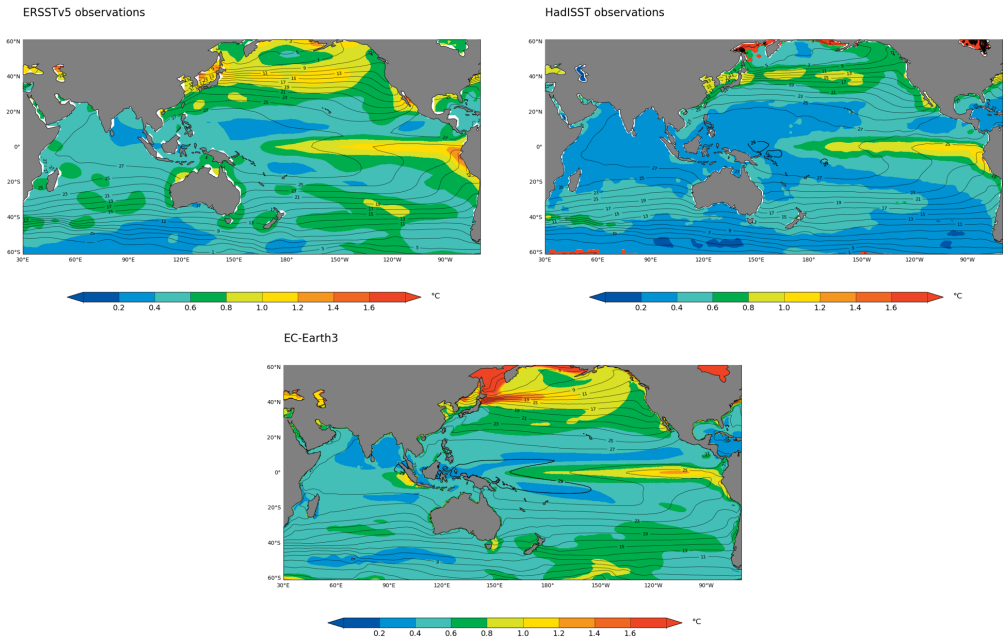

Figure 5.1: Climatological annual mean SST (contoured every 2°C beginning at 5°C; the thick contour is 29°C) and standard deviation of monthly SST anomalies (°C, color shading) from detrended observations (ERSSTv5, 1870–2024; HadISST, 1870-2024) and multicentury preindustrial control integration of EC-Earth3.

After establishing the general performance over the Indo-Pacific basin, the analysis focuses on the Niño-3.4 region, a key index for monitoring and quantifying ENSO-related SST variability. The climatological annual cycle of SST anomalies in the Niño-3.4 region (Figure 5.3) illustrates the mean intra-annual modulation of SST in the central equatorial Pacific. Both observations display coherent seasonal evolution, with positive anomalies increasing from boreal winter and early spring, peaking in late spring to early summer, and declining toward autumn. EC-Earth3 successfully reproduces the general timing and shape of this cycle, capturing the transition between warm and cool phases. However, it exhibits slightly lower amplitudes during boreal spring and a more gradual cooling afterward.

The extended Niño-3.4 index record (Figure 5.4) further demonstrates that EC-Earth3 reproduces realistic SST anomaly variability in the equatorial Pacific over the 500-year preindustrial control integration. Both observational datasets display comparable amplitude and frequency of events, providing a robust benchmark for

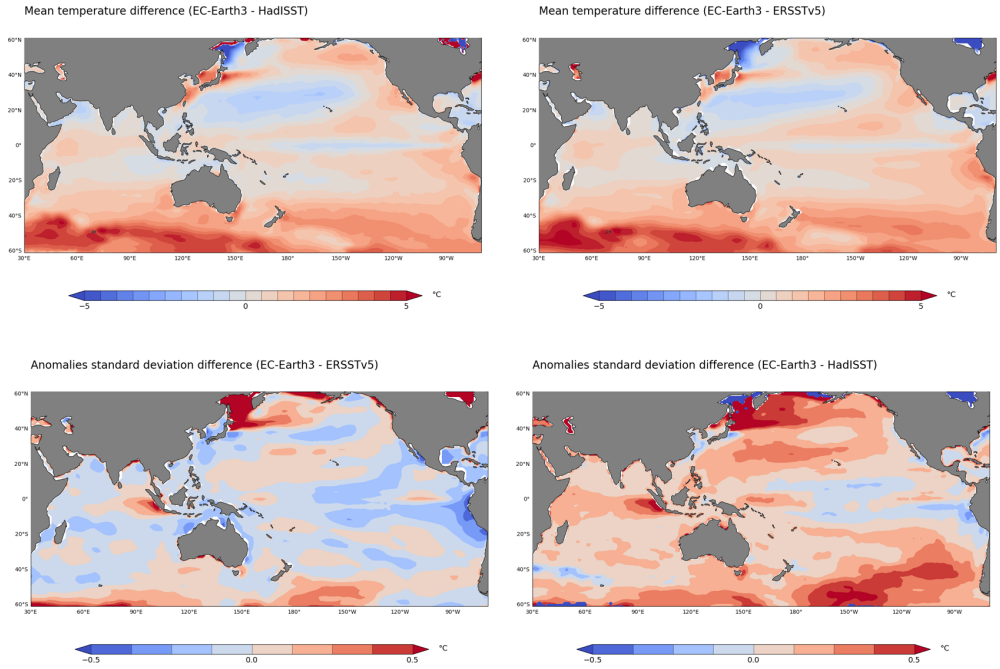

Figure 5.2: Climatological annual mean SST differences and standard deviation of monthly SST anomalies differences from detrended observations (ERSSTv5, 1870-2024; HadISST, 1870-2024) and multicentury preindustrial control integration of EC-Earth3.

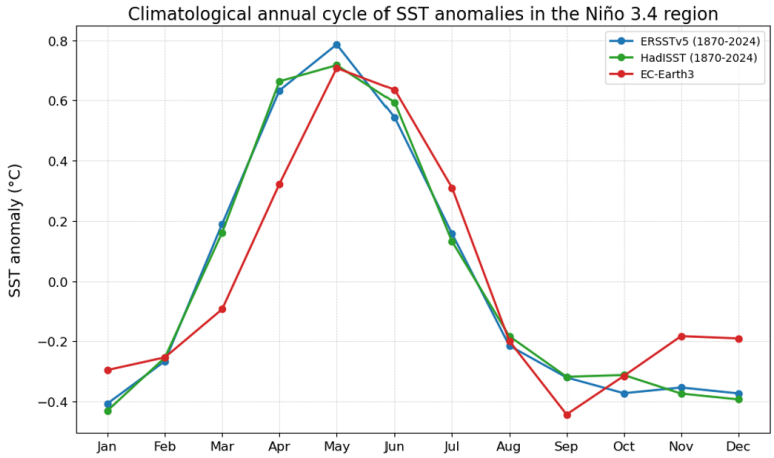

Figure 5.3: Climatological annual cycle of Niño-3.4 SST anomalies computed from detrended observations (ERSSTv5, 1870-2024; HadISST, 1870-2024) and from the 500-year EC-Earth3 preindustrial control simulation.

model evaluation. The simulated series exhibits irregular oscillations of varying intensity and duration, including interannual to multidecadal modulation, closely resembling natural ENSO variability. The strongest simulated events exceed +3°C, while moderate ones range between 1°C and 1.5°C, consistent with the magnitude of observed Niño-3.4 anomalies. However, the overall variability amplitude is slightly weaker: the Niño-3.4 index standard deviation over the whole simulation is 0.68°C, compared with 0.80 °C in ERSSTv5 and 0.74°C in HadISST. This systematic underestimation suggests that, although the model reproduces the diversity and irregularity of ENSO events, their amplitude is somewhat damped.

Spectral analysis reinforces these findings (Figure 5.5). Observations show a well-defined peak around 3.5 years, corresponding to the canonical ENSO timescale, and a secondary enhancement between 5 and 8 years associated with lower-frequency variability. EC-Earth3 successfully captures the dominant 3-4 year peak, demonstrating that the principal oscillatory mode of ENSO is well simulated. However, the model spectrum shows reduced power in the 5-8 year band and lower overall spectral amplitude across all frequencies, suggesting that the simulated ENSO variability is weaker and less energetic at interannual to decadal timescales. A similar underestimation of ENSO spectral power has been documented in other coupled models and has been linked to insufficient atmospheric noise forcing. As shown by Yang et al. (2019), the inclusion of stochastic physics in the atmospheric component enhances the temporal variability of ENSO, leading to the emergence of distinct peaks at periods of 3-4 and 5-7 years, in closer agreement with observations.

The temporal persistence of ENSO events is well described by the autocorrelation of the Niño-3.4 index (Figure 5.6). Starting from the December value (Dec^0), both observations and EC-Earth3 exhibit a rapid decay of correlation within the first year and a transition to negative correlations at approximately ±2 years, consistent with the typical ENSO phase-reversal timescale. The shape and amplitude of the EC-Earth3 curve closely match those of ERSSTv5 and HadISST, although the model displays slightly weaker negative correlations and a marginally faster loss of persistence. These features suggest that ENSO events in EC-Earth3 tend to dissipate somewhat faster than observed, but the general phasing and memory of the oscillation are credibly represented.

The seasonal dependence of Niño-3.4 variability (Figure 5.7) further validates the

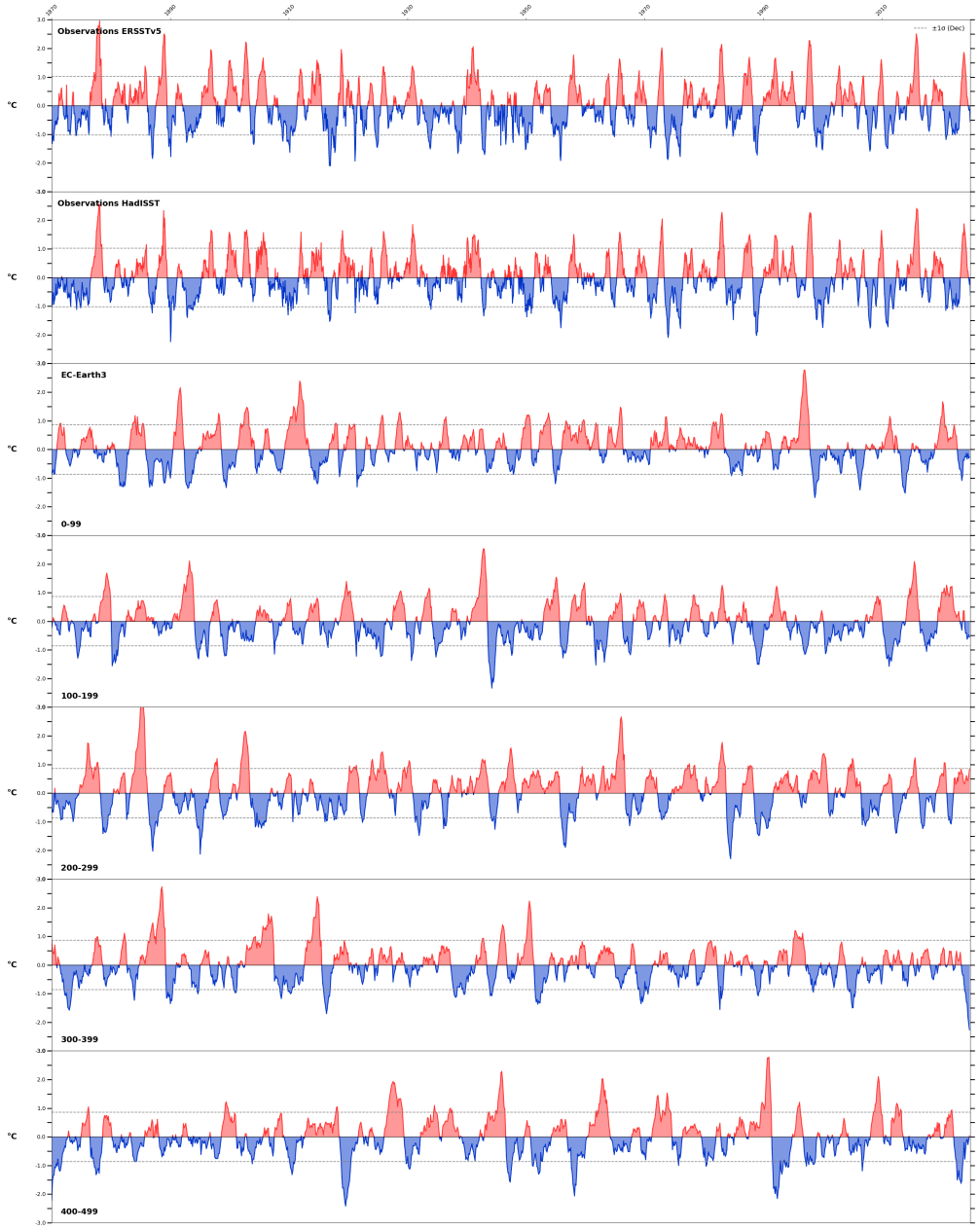

Figure 5.4: The Niño-3.4 SST index from (first panel) detrended ERSSTv5 observations during 1870–2024, (second panel) detrended HadISST observations during 1870-2024 and (remaining panels) the 500-year EC-Earth3 preindustrial control integration. Each row shows each subsequent 100-year period as marked. Two horizontal lines show the +1 and -1 std computed only for December anomalies.

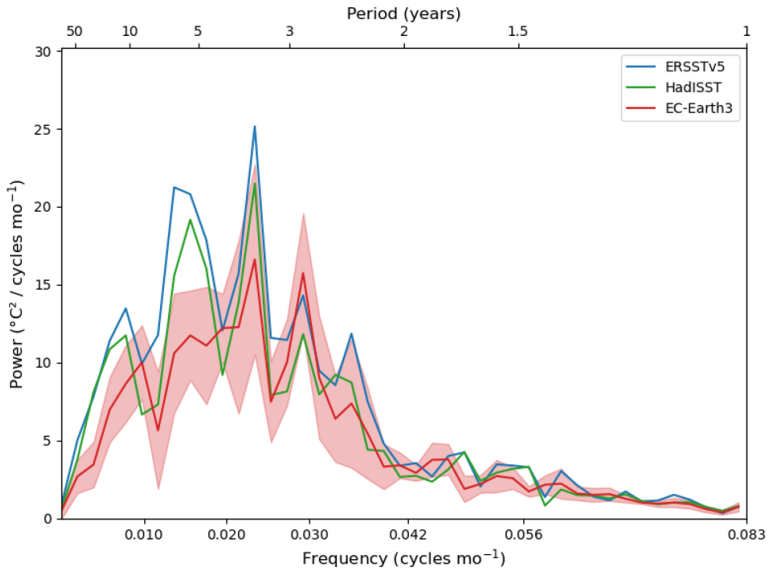

Figure 5.5: Power spectrum of the Niño-3.4 SST index from detrended observations (ERSSTv5, 1870-2024; HadISST, 1870-2024) and EC-Earth3 (500 years). The light-red shading depicts the confidence intervals (95%) for the EC-Earth3 spectrum based on the individual spectra for each 100-year segment.

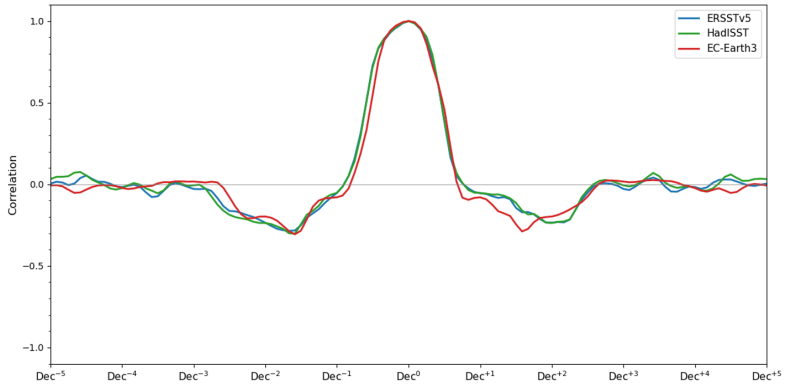

Figure 5.6: Monthly autocorrelation curves of the Niño-3.4 SST index from observations (detrended ERSSTv5, 1870-2024; HadISST 1870-2024) and EC-Earth3. Autocorrelations are computed from the December Niño-3.4 index (Dec^0) and span the previous and subsequent 5 years.

model. In the observations, the standard deviation follows a well-defined annual cycle, with a minimum during boreal summer (June-July) and a maximum during

boreal winter (November–December). This seasonal modulation reflects the well-known phase-locking of ENSO to the annual cycle, whereby El Niño and La Niña events tend to develop during boreal spring, peak toward the end of the year, and decay in the following spring (Rasmusson & Carpenter, 1982). EC-Earth3 reproduces this phase relationship, capturing the timing of the maximum variability but systematically underestimating its amplitude throughout the year. The observed maxima of 1.02°C (ERSSTv5) and 0.95°C (HadISST) contrast with the model's peak of 0.86°C (in January, with a one-month lag), indicating a weaker representation of warm-event intensity. This underestimation is consistent with the reduced variance identified in both the time-domain and spectral analyses, suggesting that ENSO variability in EC-Earth3 is slightly damped. A similar amplitude bias has been reported by Yang et al. (2019), who showed that the introduction of stochastic atmospheric physics in EC-Earth3 can enhance the model's ENSO-related variability and improve the representation of the monthly standard deviation of the Niño-3.4 index.

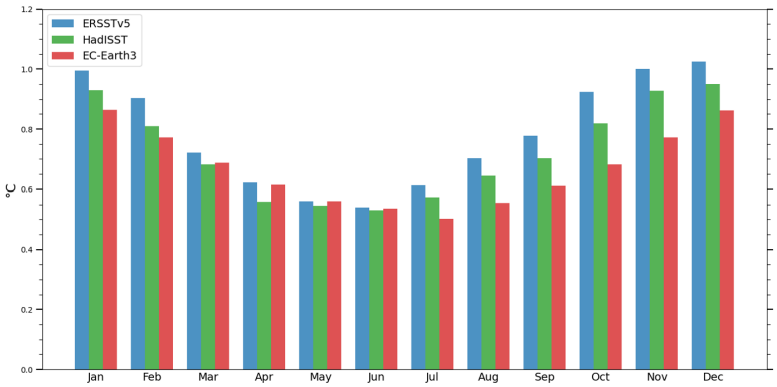

Figure 5.7: Monthly standard deviation of the Niño-3.4 SST index for detrended observations (ERSSTv5, 1870–2024; HadISST, 1870-2024) and EC-Earth3 (500 years).

Finally, the 30-year running standard deviation of the Niño-3.4 index (Figure 5.8) illustrates the multidecadal modulation of ENSO amplitude. Both observational datasets show distinct periods of weaker variability, such as the early 20^{th} century, and more active phases, such as the late 20^{th} century. This increase in ENSO activity during the latter part of the century is also clearly visible in the Niño-3.4 time series (Figure 5.4), where large-amplitude events become more frequent after the

1970s. Such an intensification of ENSO variability has been widely documented in the literature (e.g., Capotondi & Sardeshmukh, 2017). EC-Earth3 reproduces this alternating pattern of low- and high-amplitude epochs, confirming that the model generates intrinsic low-frequency modulation consistent with the observed behavior. However, the simulated standard deviation rarely exceeds the upper bound of the observational range and more frequently falls below the mean, indicating that the model's ENSO remains slightly muted even at longer timescales.

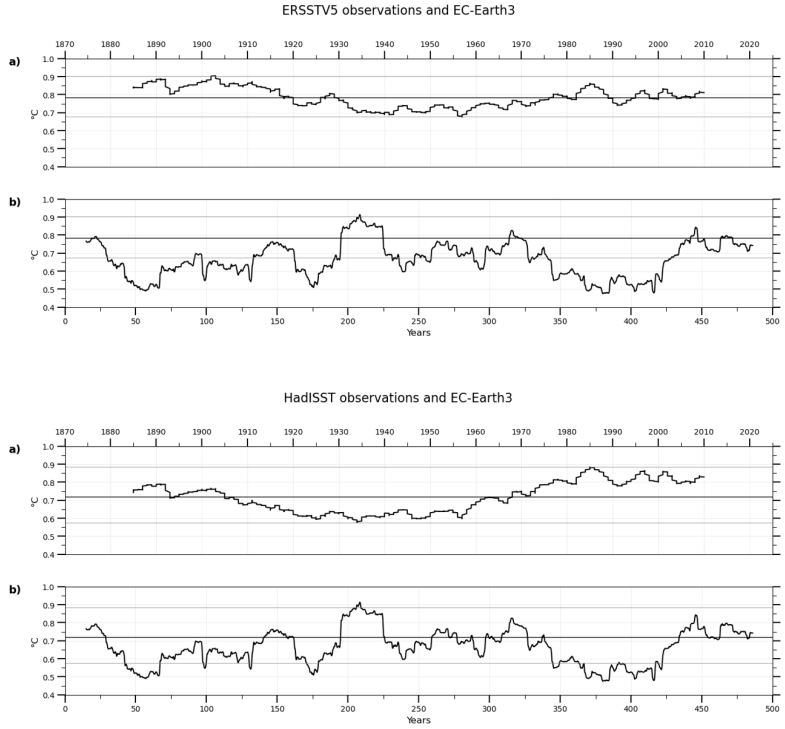

Figure 5.8: Standard deviation of the Niño-3.4 SST index computed over running 30-year periods from (a) detrended observations (ERSSTv5, 1870-2024, top panel and HadISST, 1870-2024, bottom panel) and (b) the 500-year EC-Earth3 preindustrial control simulation. Horizontal lines mark the observed mean and the range of variability.

Overall, these analyses demonstrate that EC-Earth3 provides a credible simulation of ENSO variability. The model accurately reproduces the mean SST structure of the tropical Pacific, the spatial organization and timing of interannual fluctuations,

and the dominant ENSO periodicity. Minor but systematic amplitude underestimations appear across monthly, interannual, and multidecadal scales, leading to a somewhat weaker ENSO than observed. Despite this damping, EC-Earth3 captures the essential behavior, phase evolution, and low-frequency modulation of ENSO, confirming its reliability in representing the dynamics of the tropical Pacific climate system.

5.1.2 Composite El Niño and La Niña events

The composite analysis of El Niño and La Niña events provides deeper insight into the spatial and temporal evolution of ENSO-related SST anomalies. Observational composites for the period 1870-2024 include 26 El Niño and 17 La Niña events, whereas the 500-year EC-Earth3 control simulation identifies 80 El Niño events and 75 La Niña events, offering a statistically robust foundation for evaluating model performance.

Hovmöller diagrams in Figure 5.9 reveal that observed El Niño events originate in the central-to-eastern equatorial Pacific during boreal summer, intensify through autumn, and reach their peak toward the end of the calendar year, with maximum SST anomalies exceeding +2°C between 150°W and 100°W. La Niña events display a comparable temporal evolution but with distinct asymmetries: the maximum cold anomalies are located farther west (around 170°W-110°W), and their spatial structure is more diffuse. Moreover, cold anomalies tend to persist longer into the subsequent year, often reintensifying during the following winter. This persistence, contrasted with the rapid decay of El Niño events after their peak, exemplifies the well-documented asymmetry in ENSO evolution described by Okumura and Deser (2010). While both phases typically develop in late boreal spring or summer and peak in winter, El Niños decay rapidly by the following summer, whereas La Niñas frequently persist or re-emerge, reflecting nonlinear ocean–atmosphere feedbacks that favor longer-lived cold events.

EC-Earth3 reproduces the main features of these observed composites, including the correct seasonal timing and the east–west contrast between warm and cold phases (Figure 5.9). The model captures the onset of SST anomalies in boreal spring, their amplification toward December, and their decay during the subsequent spring. However, some systematic differences are evident. During El Niño, EC-Earth3

produces a more diffuse warming pattern that extends farther west into the central Pacific, with slightly weaker peak amplitudes in the eastern basin. During La Niña, the model underestimates the intensity of cold anomalies, typically remaining above -1.5°C, and simulates a broader, less concentrated cooling pattern. A notable limitation is the lack of persistence of cold anomalies in the eastern Pacific after the spring following the La Niña peak, indicating that the model struggles to sustain negative SST anomalies beyond one year. This limitation contributes to a weaker asymmetry between El Niño and La Niña in EC-Earth3 compared to observations, consistent with the biases identified by Yang et al. (2019).

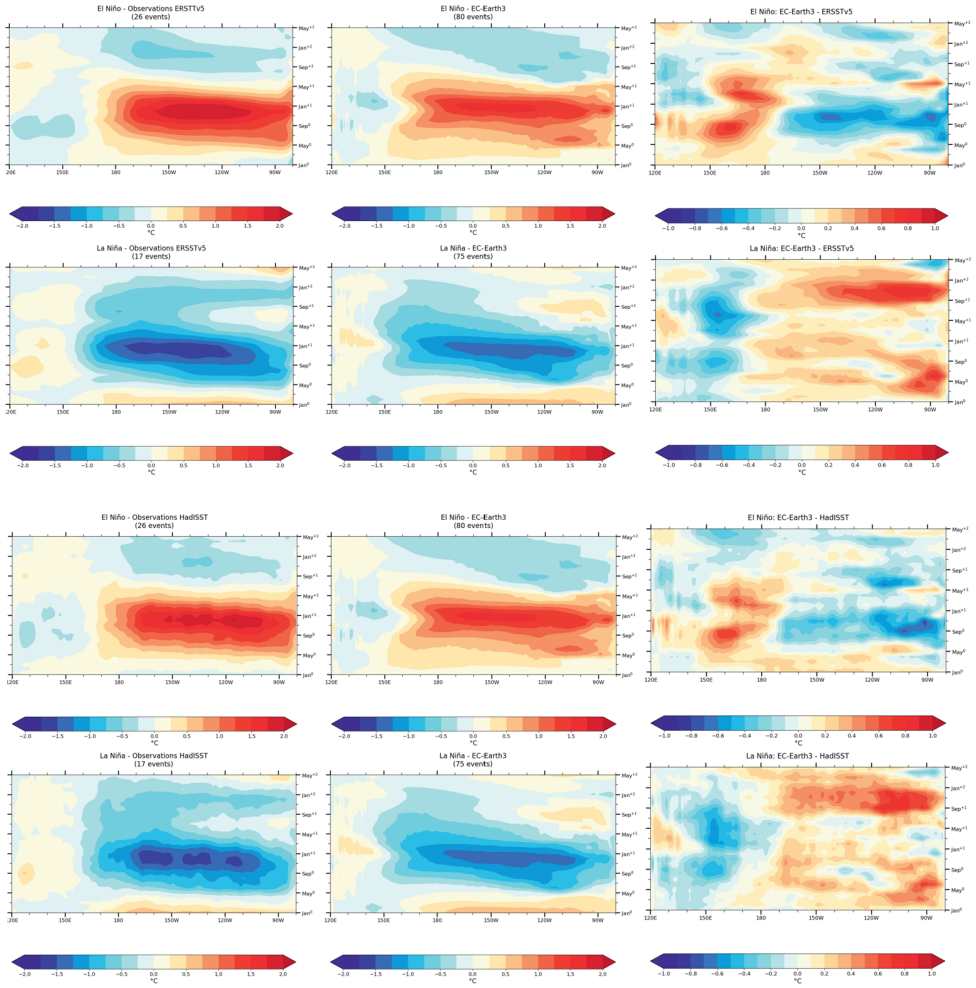

Figure 5.9: Longitude–time sections of composite SST anomalies along the equator (3°N–3°S) for El Niño and La Niña based on observations (ERSSTv5, 1870-2024; HadISST, 1870-2024) and EC-Earth (500 years), along with their differences.

The observed composites in Figure 5.10 illustrate the coupled evolution of SST, precipitation, thermocline depth, and surface wind anomalies throughout the ENSO lifecycle. During El Niño development (MAM^0-SON^0), warm SST anomalies first appear in the central equatorial Pacific and progressively intensify and extend eastward, reaching their maximum amplitude ($> +2°C$) during boreal winter (DJF^0). This surface warming is accompanied by enhanced convection and positive precipitation anomalies over the central–eastern Pacific, while subsidence and drying dominate the western Pacific and Maritime Continent. In the subsurface, a deepened thermocline in the east and a shoaled thermocline in the west reflect the characteristic flattening of the equatorial thermocline slope, consistent with westerly surface wind anomalies over the central Pacific. As the event decays (MAM^{+1}-JJA^{+1}), negative thermocline anomalies propagate eastward, initiating the transition toward La Niña conditions.

In contrast, La Niña composites exhibit cold SST anomalies that emerge in the central Pacific during boreal summer, strengthen through autumn, and peak between DJF^0 and MAM^{+1} with amplitudes below –2°C. The associated rainfall pattern shows enhanced convection over the western Pacific and suppressed precipitation in the central-eastern basin. Subsurface conditions reveal a mirror-like thermocline response, with shoaling in the east and deepening in the west, maintained by persistent easterly wind anomalies. However, the decay of La Niña events differs from that of El Niño: negative SST and thermocline anomalies tend to persist or even reintensify into the following winter (DJF^{+1}), confirming the well-known asymmetry between warm and cold ENSO phases described by Okumura and Deser (2010).

EC-Earth3 generally reproduces the main features of this observed ENSO evolution (Figure 5.11), including the correct seasonal phasing, the east-west contrast in SST anomalies, and the associated atmospheric and subsurface responses. Nonetheless, systematic differences are evident. The model simulates a more diffuse and westward-extended pattern of SST anomalies, with weaker warming in the eastern Pacific during El Niño and a less pronounced cooling in the central–eastern Pacific during La Niña. The associated precipitation anomalies mirror this bias, showing a westward-displaced convective center and overly strong drying over the Maritime Continent.

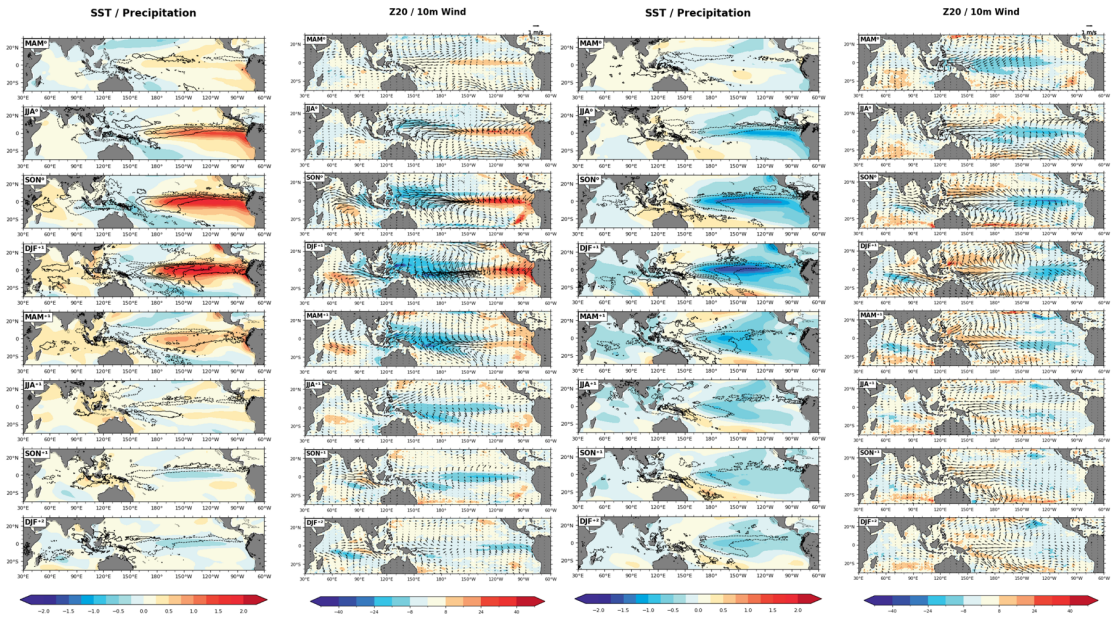

Figure 5.10: Observed (ERA5, 1940-2024 and 1954-2024 for thermocline) El Niño (left) and La Niña (right) seasonal composite evolution for SST and precipitation anomalies and thermocline depth (Z20) and 10m wind anomalies. SST (°C) and Z20 (m) are shaded; precipitation contours (solid for positive anomalies, dashed for negative anomalies) are ±9, ±7, ±5, ±3, ±1 mm/day, and the wind vector scale (m/s) is shown at the top of the figure.

In terms of subsurface and wind responses, EC-Earth3 qualitatively captures the characteristic thermocline flattening during El Niño and the opposite configuration during La Niña. However, the amplitude of these thermocline anomalies is reduced compared to observations, with an underestimation of the deepening in the east and an overestimation of the shoaling in the west. This distortion is accompanied by excessively strong westerly wind anomalies during El Niño and a weaker easterly response during La Niña. As a consequence, the model tends to underestimate the overall ENSO amplitude and to shorten the persistence of cold anomalies beyond one year, leading to a weaker expression of the observed ENSO asymmetry.
In summary, the composite analysis confirms that EC-Earth3 provides a dynamically consistent representation of ENSO evolution and its coupled ocean–atmosphere feedbacks. The model realistically captures the timing, spatial structure, and phase transition of El Niño and La Niña events, as well as the associated thermocline–wind

coupling that underpins the Bjerknes feedback. Quantitative differences remain, notably a modest underestimation of anomaly amplitudes, a westward displacement of the maximum SST and precipitation signals, and a reduced persistence of cold events. These biases result in a slightly weaker and more symmetric ENSO than observed, consistent with findings from previous EC-Earth assessments. Nevertheless, the overall agreement with observations demonstrates that the model can be considered a reliable framework for the experiments presented in the following chapter, aimed at exploring the mechanisms and impacts of ENSO variability under controlled perturbations.

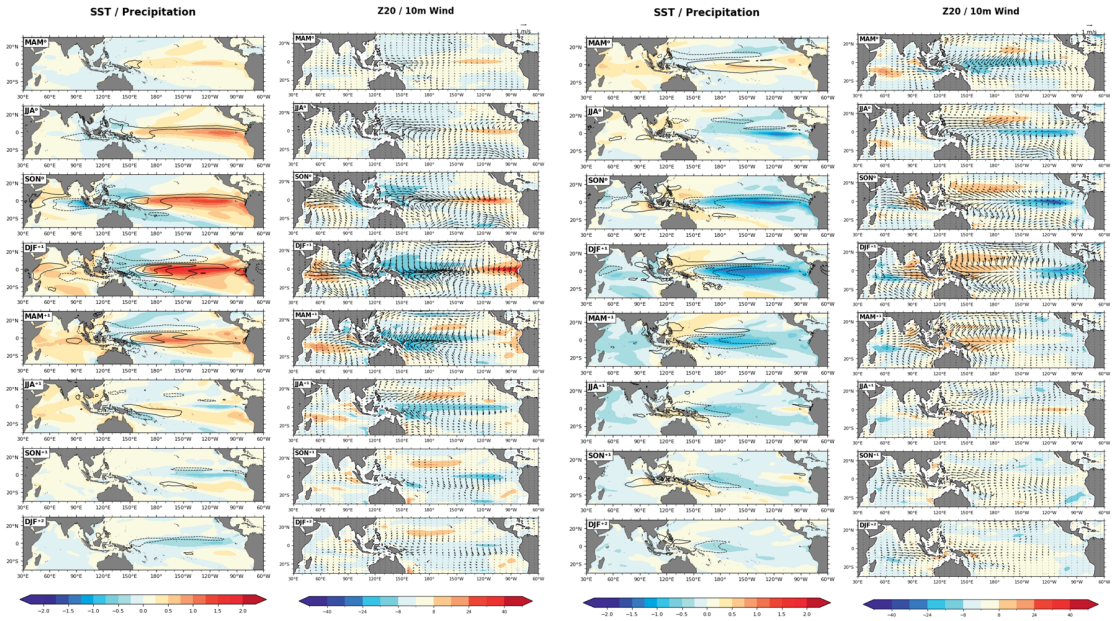

Figure 5.11: EC-Earth3 (500-year) El Niño (left) and La Niña (right) seasonal composite evolution for SST and precipitation anomalies and thermocline depth (Z20) and 10m wind anomalies. SST (°C) and Z20 (m) are shaded; precipitation contours (solid for positive anomalies, dashed for negative anomalies) are ±9, ±7, ±5, ±3, ±1 mm/day, and the wind vector scale (m/s) is shown at the top of the figure.

5.2 Response of ENSO to weakened AMOC in a preindustrial and in a 4xCO$_2$ climate

5.2.1 Niño-3.4 SST variability

Building upon the evaluation of ENSO representation in EC-Earth3, this section investigates how ENSO responds to an AMOC weakening under both preindustrial and 4xCO$_2$ climate conditions. The analysis follows the same methodological framework used for the model–observation comparison but is here applied to contrasting model experiments, with the aim of identifying changes in ENSO amplitude, spatial structure, and coupled ocean–atmosphere feedbacks. Conducting the analysis in parallel for the two climatic backgrounds enables a direct assessment of how the AMOC–ENSO linkage depends on the mean state of the climate system.

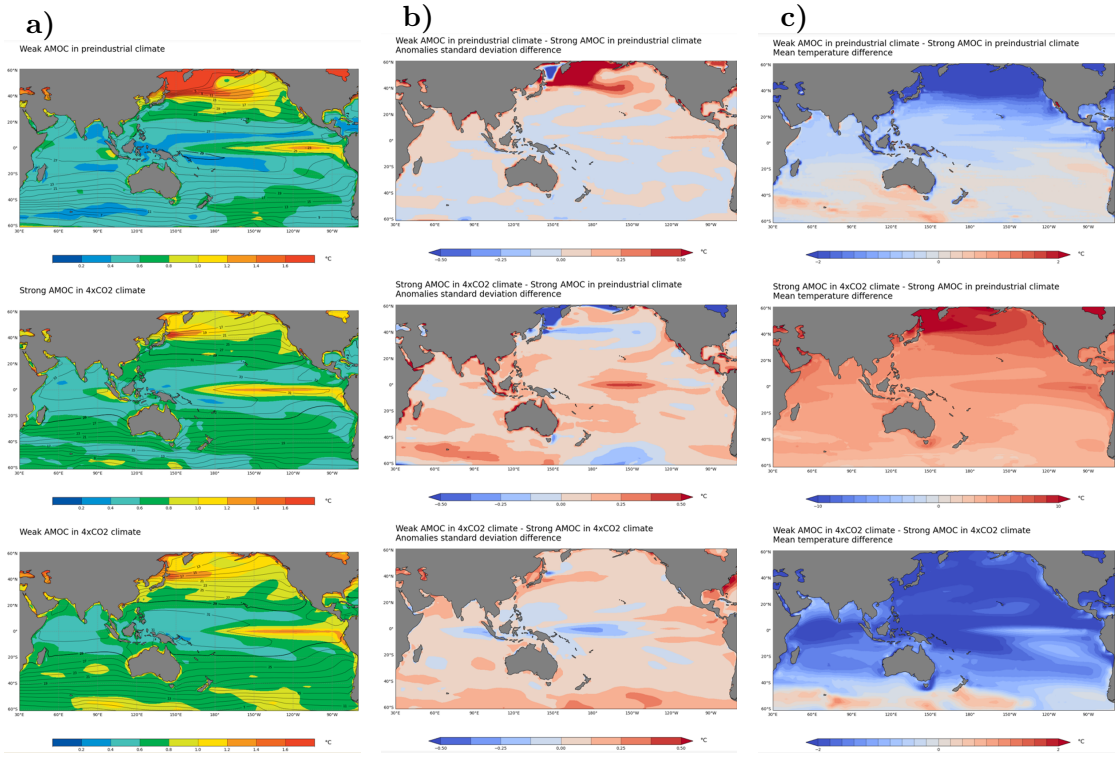

Figure 5.12: a) Climatological annual mean SST (contoured every 2°C beginning at 5°C; the thick contour is 29°C) and standard deviation of monthly SST anomalies (°C, color shading) from EC-Earth3 experiments. b) Climatological annual mean SST differences from EC-Earth3 experiments. c) Standard deviation of monthly SST anomalies differences from EC-Earth3 experiments.

A basin-scale perspective is first adopted to examine how AMOC weakening influences the large-scale SST distribution and variability under different CO_2 backgrounds. Figure 5.12 illustrates the climatological annual mean SST and the variability of monthly SST anomalies derived from the EC-Earth3 experiments, together with the inter-simulation differences. Under preindustrial conditions (top row), the comparison between weak and strong AMOC states reveals the characteristic interhemispheric dipole extensively reported in previous studies (e.g., Dong & Sutton, 2007), with widespread cooling across the Northern Hemisphere and a more moderate warming in the Southern Hemisphere. This thermal contrast is particularly evident in the eastern tropical Pacific. Within this background change, the variability of SST anomalies exhibits a modest increase in the eastern equatorial Pacific, accompanied by a slight westward extension of the main variability center. Farther west, however, a localized reduction in variability emerges.

To isolate the respective influences of greenhouse forcing and AMOC variability, the analysis is next extended to the $4\times CO_2$ experiments. This comparison allows the disentangling of the direct radiative warming effects from those induced by AMOC weakening, thereby clarifying their individual roles in shaping ENSO-related SST variability. In the presence of a strong AMOC, elevated CO_2 concentrations induce substantial warming throughout the basin relative to preindustrial conditions, consistent with the expected radiative forcing response. This warming is particularly pronounced in the eastern equatorial region, where the cold tongue characteristic of the preindustrial climate warms by up to 5-6°C, resulting in a weakened zonal SST gradient. Within this warmer background, the variability of SST anomalies intensifies across the central equatorial Pacific, where it already peaks under preindustrial conditions. Notably, the region of maximum variability extends farther west, approaching the coasts of Papua New Guinea. This pattern suggests that greenhouse forcing alone tends to amplify ENSO-related fluctuations while shifting their center of action westward toward the central Pacific. When the AMOC weakens within the $4\times CO_2$ climate, the response pattern changes substantially. Despite the overall warmer mean state, SSTs decrease across much of the basin, reflecting the compensating cooling effect associated with the AMOC slowdown. This cooling is most pronounced over the central and western Pacific, while in the eastern equatorial region it remains weaker, with surface temperatures staying

relatively high. At the same time, the variability of SST anomalies intensifies across much of the basin, while the tongue of high-variability becomes less extended westward than in the strong-AMOC case and more pronounced in the eastern Pacific.

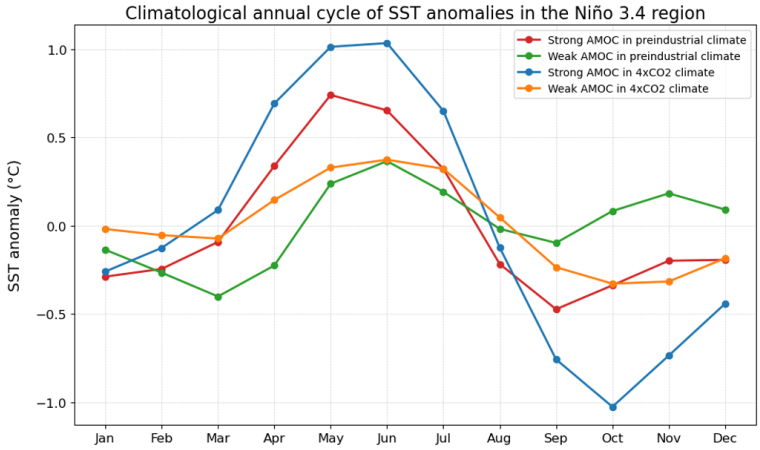

Figure 5.13: Climatological annual cycle of Niño-3.4 SST anomalies from EC-Earth3 experiments.

Moving to the Niño 3.4 region, Figure 5.13 presents the climatological annual cycle of SST anomalies, providing insight into the seasonal modulation of equatorial Pacific temperatures under different AMOC strengths and greenhouse gas forcings. The amplitude of this cycle serves as a key diagnostic of the seasonal forcing acting on ENSO dynamics. Under preindustrial conditions, both AMOC states exhibit a clear seasonal oscillation, with SSTs peaking in late boreal spring and reaching a minimum in late summer to early autumn. The weak-AMOC case, however, displays a noticeably smaller amplitude, reflecting a reduced seasonal contrast in equatorial Pacific temperatures. This behavior is consistent with previous modeling studies (e.g., Dong & Sutton, 2007; Liu et al., 2023; Timmermann et al., 2007), which associated AMOC weakening with a diminished SST annual cycle in the equatorial Pacific.

In the 4×CO_2 climate, maintaining a strong AMOC substantially increases the annual cycle amplitude, with positive anomalies exceeding +1°C in early boreal summer and pronounced negative anomalies (below -1°C) emerging in boreal autumn. When the AMOC weakens in this warmer background, the amplitude of

the SST annual cycle is substantially reduced, producing the flattest curve among all simulations. This result aligns with Liu et al. (2023), who found that a weakened AMOC under greenhouse forcing suppresses the amplitude of the equatorial Pacific SST annual cycle, thereby reducing the strength of the seasonal modulation that influences ENSO dynamics.

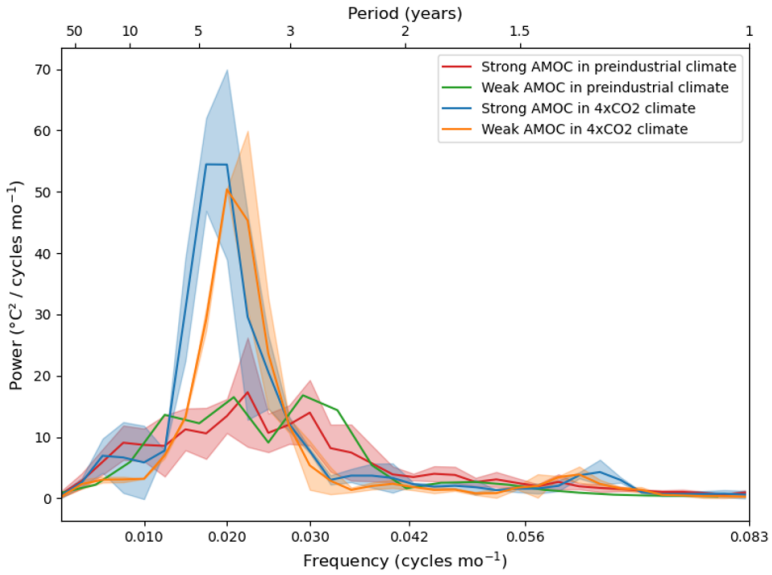

Figure 5.14: Power spectrum of the Niño-3.4 SST index from EC-Earth3 experiments. The shadings depict the confidence intervals (95%) based on the individual spectra for each 100-year segment.

The power spectrum of Niño 3.4 SST anomalies provides a quantitative assessment of ENSO variability across different timescales, allowing changes in both amplitude and dominant frequency to be evaluated. Figure 5.14 compares the Niño 3.4 power spectra for the four EC-Earth3 experiments, illustrating how ENSO periodicity and intensity respond to both greenhouse forcing and AMOC changes. Under preindustrial conditions, the spectra reveal that ENSO variability in both AMOC states peaks at similar frequencies, corresponding to periods of approximately 3–5 years, indicating that the dominant ENSO timescale remains essentially unchanged. However, the weak-AMOC simulation displays slightly higher spectral power across much of the 0.01–0.04 cycles-per-month range, suggesting a modest amplification of ENSO amplitude when the AMOC is reduced. Although this enhancement is

relatively small and falls within the uncertainty range, it indicates a tendency for weakly intensified variability under a reduced AMOC. These results are consistent with previous studies (Dong & Sutton, 2007; Timmermann et al., 2007), which linked AMOC weakening to moderate changes in ENSO strength rather than its characteristic period.

To assess the combined influence of greenhouse forcing and AMOC weakening, the spectra are next compared across the preindustrial and $4\times CO_2$ climates under both strong and weak AMOC states. In all experiments, ENSO variability continues to peak at similar frequencies (3-5 years), confirming that the dominant timescale is largely preserved. In contrast, the amplitude of variability differs substantially among configurations. Under $4\times CO_2$ forcing, spectral power increases markedly, particularly in the strong-AMOC case, indicating an intensification of ENSO activity in a warmer climate. When the AMOC is weakened, ENSO power remains above preindustrial levels but is slightly lower than in the strong-AMOC $4\times CO_2$ case, suggesting that AMOC weakening exerts a moderating influence on the greenhouse-driven amplification of ENSO. A minor shift of the spectral peak toward longer periods ($\sim$5 years) under global warming further hints at a modest lengthening of the ENSO cycle, though this tendency is less evident when the AMOC is weak. This behavior contrasts with the results of Liu et al. (2023), who found that anthropogenic warming under the RCP8.5 scenario slightly shortens the ENSO period, and that an AMOC slowdown further reduces it. Liu also reported a decrease in the magnitude of ENSO variability over the twenty-first century, with a weakened AMOC under global warming acting to amplify variability relative to this reduced future state.

Figure 5.15 illustrates the seasonal evolution of Niño 3.4 SST anomaly standard deviation across the different experiments, along with the inter-simulation differences. In the preindustrial climate, the weak-AMOC simulation reveals a modest reorganization of the seasonal cycle: variability increases from late winter to early summer, reaching slightly higher values between March and May, while it decreases from late summer through early winter, although winter remains the season of maximum variability. These seasonal differences nearly compensate each other, resulting in a comparable overall amplitude of variability between the two preindustrial simulations, with basin-mean standard deviation values of 0.678°C for the

strong-AMOC state and 0.686°C for the weak-AMOC state. This slight increase (∼1.2%) is considerably smaller than the 36% enhancement reported by Dong and Sutton (2007), who found a strong, year-round amplification of ENSO-related SST variability. The discrepancy likely arises from differences in model configuration, the magnitude of the AMOC reduction, and the spatial domain considered. While Dong and Sutton analyzed the Niño-3 region farther east, the present study targets the Niño-3.4 box, which extends westward into areas where variability changes are weaker or even opposite in sign. This interpretation is supported by Figure 5.12, which shows that the increase in SST variability under weak-AMOC conditions is mainly confined to the eastern equatorial Pacific, outside the Niño 3.4 box.

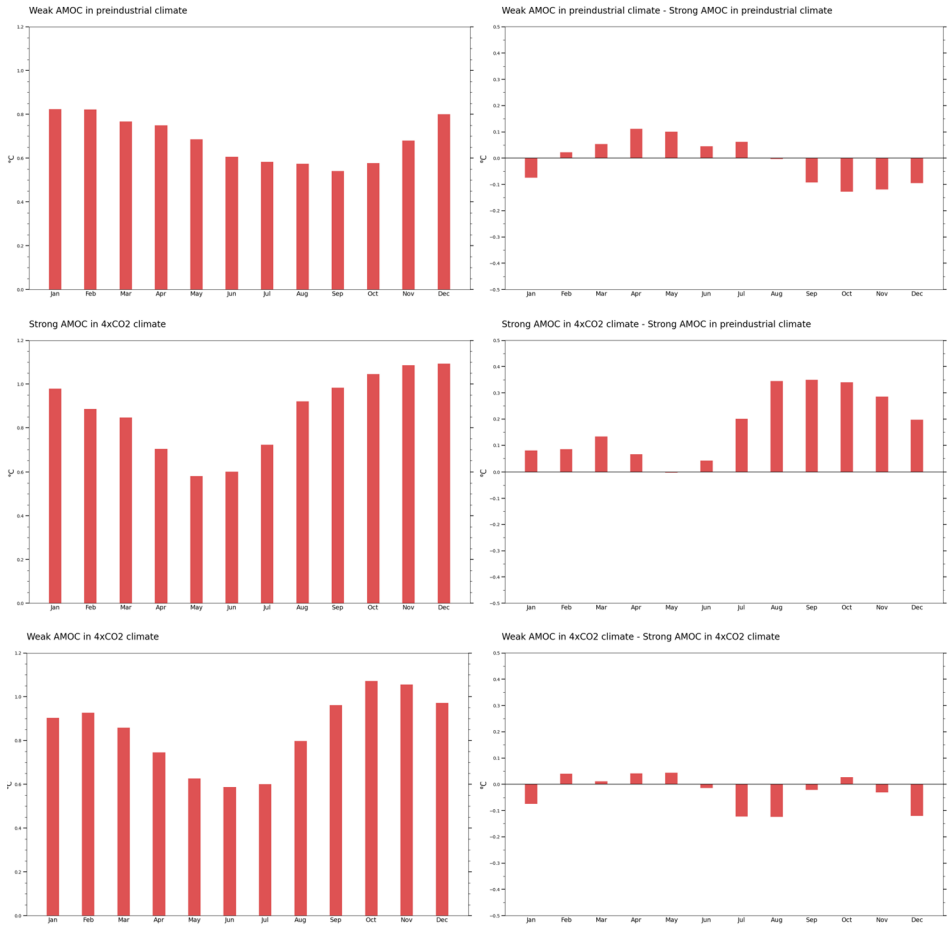

Figure 5.15: Monthly standard deviation of the Niño-3.4 SST index for EC-Earth3 experiments, along with their differences.

Both 4xCO_2 simulations exhibit enhanced variability relative to the preindustrial state, indicating that greenhouse forcing amplifies ENSO amplitude. The enhancement is most pronounced during boreal autumn and winter, consistent with a stronger and more coherent ENSO cycle in a warmer climate. When the AMOC is weakened, the overall variability remains high but is slightly reduced compared to the strong-AMOC case (0.856°C vs 0.886°C), suggesting that the slowdown of the AMOC exerts a mild damping effect on greenhouse-driven ENSO intensification. The month-to-month changes in standard deviation are not uniform, as variability slightly increases in some months and decreases in others. However, the overall seasonal pattern remains similar, with maximum values in boreal winter and a minimum around May-June.

In conclusion, the analysis of EC-Earth3 experiments reveals that greenhouse forcing and AMOC strength exert contrasting influences on ENSO dynamics. Under preindustrial conditions, a weakened AMOC slightly amplifies ENSO variability, particularly in the eastern equatorial Pacific, reflecting an increase in interannual SST anomalies despite minimal changes in the dominant periodicity. Elevated CO_2 concentrations, in contrast, enhance ENSO amplitude more substantially and extend the zone of maximum variability westward into the central Pacific, leading to a stronger and more coherent cycle. When the AMOC is weakened under 4×CO_2 forcing, it partially counteracts this greenhouse-driven enhancement, reducing ENSO intensity and slightly altering the spatial distribution of variability, while the dominant 3-5 year timescale and seasonal phase-locking remain essentially unchanged. Spectral analyses and monthly standard deviations further support this conclusion, highlighting that the AMOC provides a stabilizing feedback on ENSO under warming conditions, while its reduction in preindustrial climates can modestly increase variability.

5.2.2 Composite El Niño and La Niña events

To further investigate how the air–sea coupling and SST evolution respond to both greenhouse forcing and AMOC strength, composite analyses of El Niño and La Niña events were conducted. Figure 5.16 presents the corresponding Hovmöller diagrams, illustrating the temporal and longitudinal progression of SST anomalies along the equatorial Pacific across the different experiments.

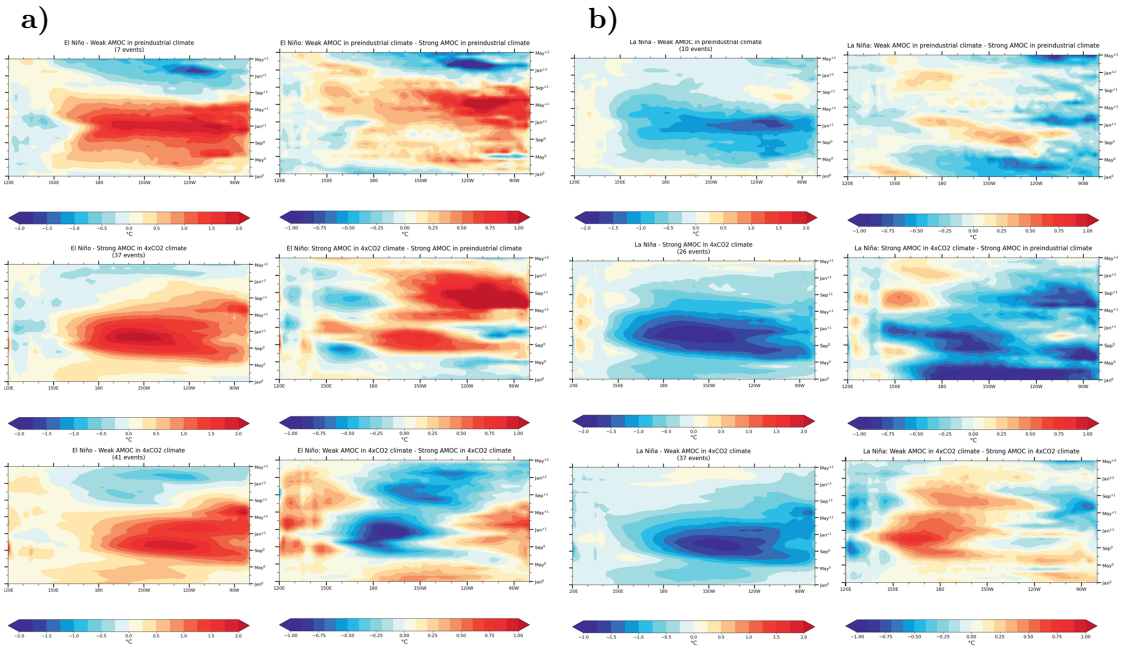

Figure 5.16: a) Longitude–time sections of composite SST anomalies along the equator (3°N–3°S) for El Niño based on EC-Earth3 experiments. b) Longitude–time sections of composite SST anomalies along the equator (3°N–3°S) for La Niña based on EC-Earth3 experiments.

For El Niño, under preindustrial conditions (Figure 5.16a, first row), a weakened AMOC produces warmer SST anomalies that emerge earlier and are more confined to the eastern Pacific, while anomalies in the central basin are comparatively weaker. The difference field highlights this eastward intensification, consistent with the modest enhancement in eastern-Pacific variability identified in Figure 5.12. This strengthening is particularly evident during the boreal spring and summer of the year following the onset of the event, whereas negative anomalies in the western Pacific strengthen about two years later, suggesting a delayed but stronger cold-phase response.

In the $4\times CO_2$ climate (Figure 5.16a, second row), strong-AMOC conditions amplify and broaden El Niño events, producing positive SST anomalies extending farther west toward the dateline and persisting into the second year after onset. This pattern reflects the combined effect of greenhouse warming and a robust AMOC, producing a stronger and more sustained El Niño signal, consistent with the trends observed in the previous analyses. When the AMOC weakens in this warmer

background (Figure 5,16a, third row), the amplitude of SST anomalies decreases slightly, and their spatial extent contracts eastward, resulting in a more localized warming pattern centered near 120°-150° W. The corresponding difference field shows pronounced negative anomalies in the central Pacific and positive ones in the far eastern and western regions, illustrating that AMOC weakening dampens the greenhouse-driven El Niño intensification in the central Pacific while enhancing warming at the basin edges.

For La Niña (Figure 5.16b, first row), under preindustrial conditions, the weak-AMOC simulation exhibits the canonical pattern, with pronounced negative SST anomalies (up to -2°C) extending across the central and eastern tropical Pacific. These cold anomalies develop almost immediately after the event onset and persist through the following months, whereas in the strong-AMOC case they emerge later, around May^0, and peak during boreal winter. The difference field indicates that AMOC weakening reduces the magnitude of negative SST anomalies in the central basin during the May^0–Jan^0 period, suggesting a partial damping of La Niña intensity.

In the 4×CO_2 climate, the strong-AMOC configuration (Figure 5.16b, second row) maintains a robust La Niña cooling pattern broadly similar to that of the preindustrial climate, but with slightly enhanced amplitude and a modest westward expansion of the cold anomalies. Negative anomalies dominate the central and eastern Pacific throughout the event, while weak positive anomalies are confined to the far-western basin. The corresponding difference plot reveals that maintaining a strong AMOC under greenhouse forcing reinforces the central-Pacific cooling up to May^{+1} and sustains pronounced negative anomalies in the eastern Pacific throughout the event's entire duration. When the AMOC weakens in the 4×CO_2 climate (Figure 5.16b, third row), La Niña events continue to exhibit significant cooling centered in the central Pacific; however, the difference field shows that these negative anomalies are weaker and more confined to the eastern part of the basin. This indicates that AMOC weakening under enhanced greenhouse forcing substantially reduces both the intensity and spatial extent of La Niña–related cooling.

As a final step, the analysis incorporates additional key variables, precipitation,

wind, and thermocline depth, to offer a comprehensive view of the AMOC's influence on ENSO dynamics. Figures 5.17 and 5.18 present the composites of SST-precipitation and wind-Z20 for El Niño and La Niña events up to two years after the event onset, focusing solely on differences between experiments to emphasize the primary changes caused by AMOC weakening.

For El Niño, under preindustrial conditions (Figure 5.17, first row), a weakened AMOC amplifies and prolongs the canonical event. Eastern-Pacific warming is enhanced and persists from MAM^{0} through the following summer (JJA^{+1}), with peak SST differences reaching +1.5°C. Precipitation patterns mirror this amplification, showing increased convective activity in the tropical Pacific. Thermocline and wind fields further support the strengthened response: the thermocline deepens in the eastern Pacific while shoaling in the west, leading to a flatter zonal profile. This effect is most pronounced in MAM^{+1}, coinciding with the maximum SST and precipitation differences. Equatorial wind anomalies evolve, starting from relatively weak differences and gradually intensifying, reaching their maximum magnitude MAM^{+1}, consistent with the changes in SST and precipitation. Taken together, these patterns suggest that, under preindustrial conditions, an AMOC weakening not only amplifies El Niño magnitude but also extends its temporal development. In the $4\times CO_2$ climate (Figure 5.17, second and third row), the influence of elevated greenhouse gases further amplifies these anomalies. In the first year following El Niño onset, warming extends into the central Pacific, and by the following year, it intensifies in the east. Precipitation, wind, and Z20 responses are coherently enhanced, favoring more extreme events. Focusing specifically on the effects of AMOC weakening in this high-CO_2 scenario, the canonical El Niño structure shifts eastward relative to the strong AMOC case. This shift is reflected in negative SST anomaly differences in the central tropical Pacific, while positive differences appear at both easternmost and westernmost extremes. Thermocline flattening and intensified easterly winds extend farther east than under strong AMOC conditions, particularly through DJF^{+1}-MAM^{+1}. Overall, these patterns indicate that AMOC weakening under elevated CO_2 shifts SST anomalies eastward while reinforcing coupled ocean–atmosphere feedbacks, producing amplified and temporally extended El Niño events.

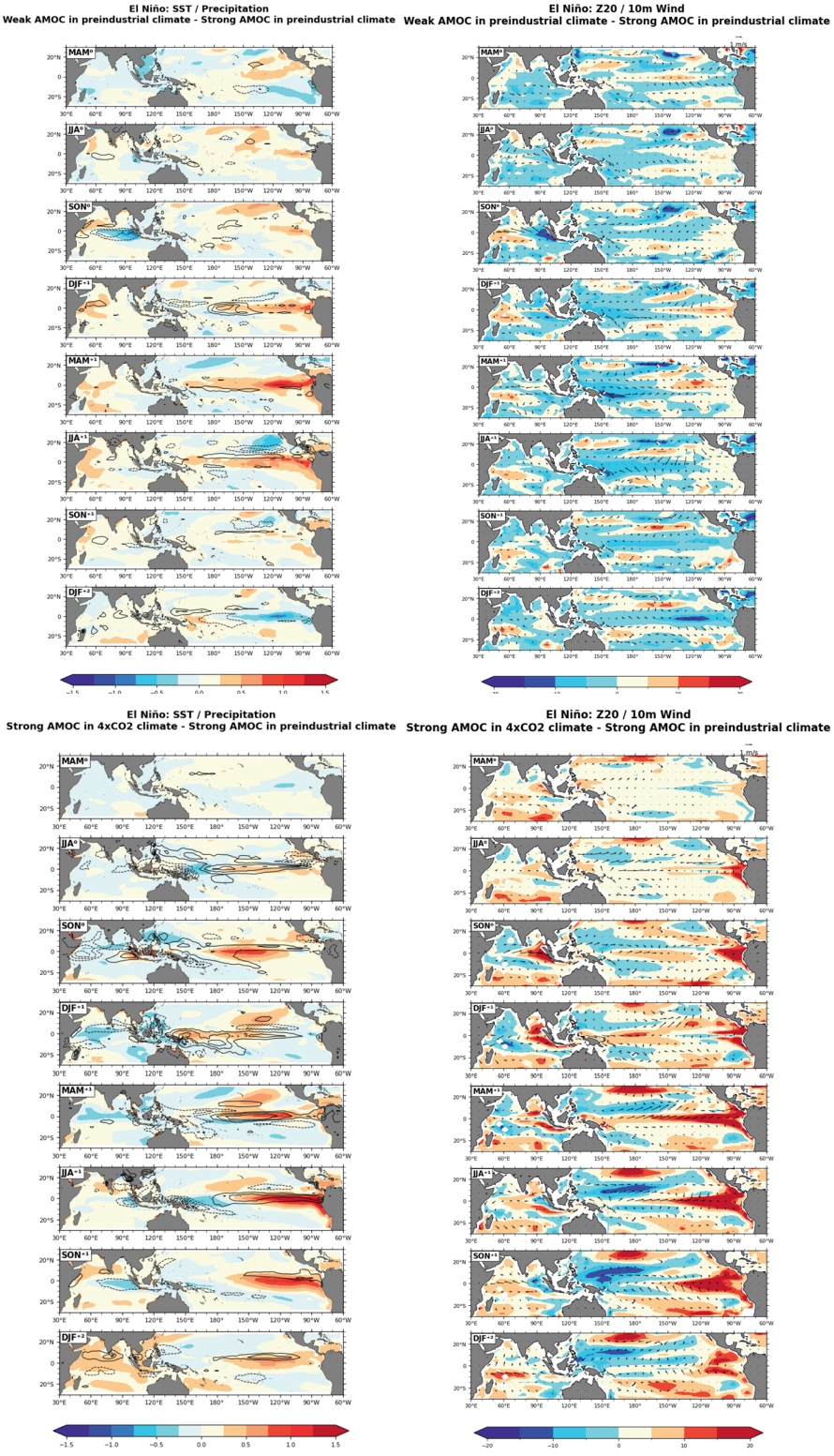
El Niño: SST / Precipitation
Weak AMOC in preindustrial climate - Strong AMOC in preindustrial climate
El Niño: Z20 / 10m Wind
Weak AMOC in preindustrial climate - Strong AMOC in preindustrial climate
El Niño: SST / Precipitation
Strong AMOC in 4xCO2 climate - Strong AMOC in preindustrial climate
El Niño: Z20 / 10m Wind
Strong AMOC in 4xCO2 climate - Strong AMOC in preindustrial climate
MAM⁰
JJA⁰
SON⁰
DJF⁺¹
MAM⁺¹
JJA⁺¹
SON⁺¹
DJF⁺²
1 m/s

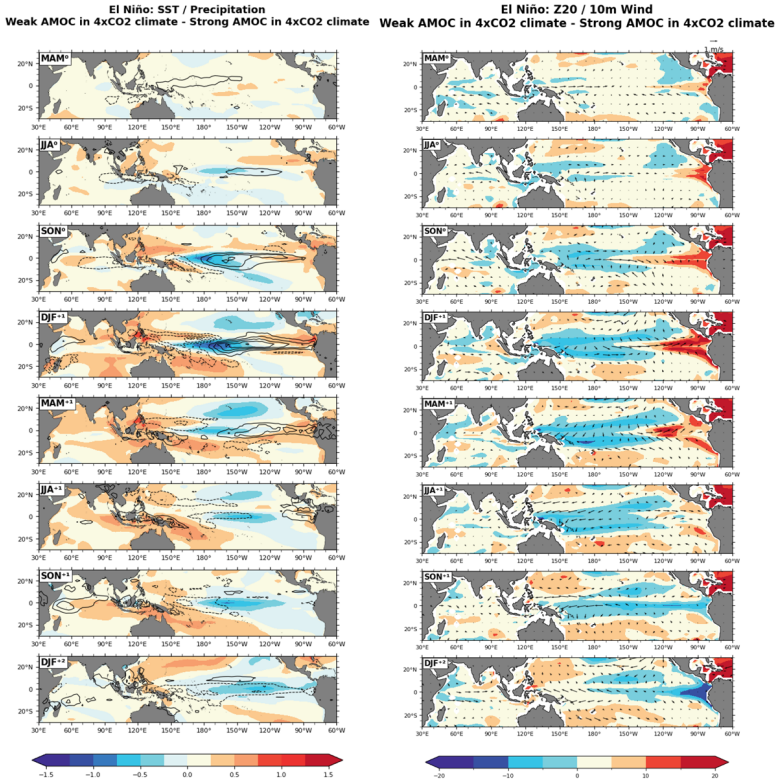

Figure 5.17: El Niño seasonal composite evolution differences across EC-Earth3 experiments starting in MAM^0 and ending in DJF^{+2} for (left) SST and precipitation anomalies and (right) thermocline depth (Z20) and 10m wind anomalies. SST (°C) and Z20 (m) are shaded; precipitation contours (solid for positive differences, dashed for negative differences) are ±5, ±4, ±3, ±2, ±1 mm/day, and the wind vector scale (m/s) is shown at the top of the figure.

Figure 5.18 presents the same set of variables for La Niña events. Under preindustrial conditions (first row), a weakening of the AMOC induces only minor modifications to the canonical La Niña patterns. SST differences are generally limited to approximately ±0.5°C, and precipitation changes are minimal. The most significant anomalies occur early in the event, when negative SST anomalies extend more strongly from east to west, consistent with Figure 5.16, where negative anomalies under weak AMOC conditions emerge immediately, in contrast with the gradual development under strong AMOC. In subsequent months, anomalies are slightly warmer or cooler, with a modest eastward extension of warmer anomalies toward the end of the considered period. Z20 and wind fields support this picture,

indicating that the overall structure and timing of La Niña events remain largely preserved under preindustrial AMOC weakening.

In the $4\times CO_2$ climate (second and third rows), La Niña events under strong AMOC conditions appear more pronounced, particularly during the first half of the period. Negative SST anomalies in the eastern Pacific intensify and expand, with a corresponding reduction in precipitation, reflecting stronger convective suppression. Wind and thermocline patterns reinforce this intensification, with strengthened westerly anomalies and a more steeply inclined thermocline. When AMOC is weakened, negative SST anomalies are reduced relative to the strong AMOC case, particularly between SON^0-MAM^{+1}, but this is accompanied by a more pronounced decrease in precipitation across the central and eastern Pacific. The wind and thermocline fields show persistent westerly anomalies and minimal changes in thermocline depth, indicating that, for La Niña, AMOC weakening exerts less impact than for El Niño, leaving the overall structure and timing of the event remaining largely preserved.

Overall, AMOC weakening has a limited effect on La Niña events. Under preindustrial conditions, changes are minor and mainly affect timing, while in the $4\times CO_2$ climate it slightly reduces the intensity and extent of cooling in the eastern Pacific, thus moderating the greenhouse-driven amplification of La Niña.

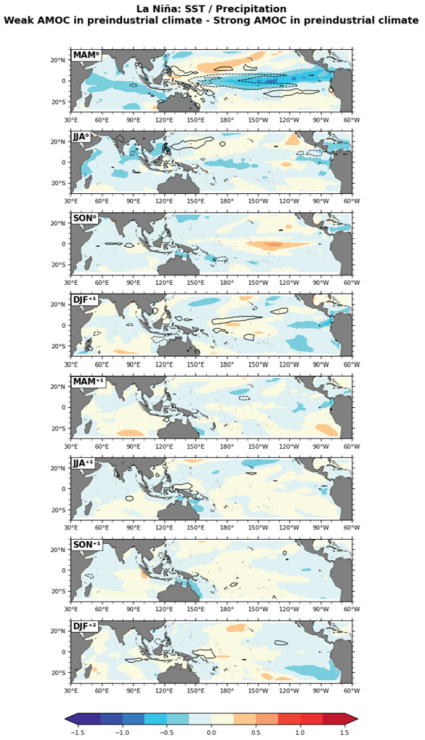
La Niña: SST / Precipitation
Weak AMOC in preindustrial climate - Strong AMOC in preindustrial climate
MAM°
JJA°
SON°
DJF°+1
MAM°+1
JJA°+1
SON°+1
DJF°+2

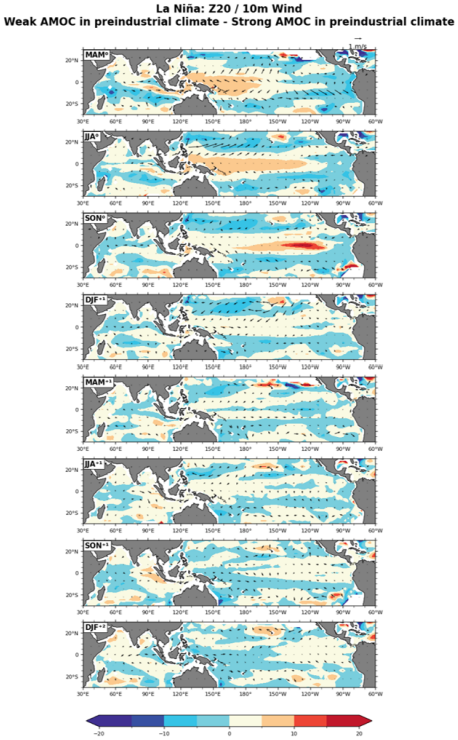
La Niña: Z20 / 10m Wind
Weak AMOC in preindustrial climate - Strong AMOC in preindustrial climate
MAM°
JJA°
SON°
DJF°+1
MAM°+1
JJA°+1
SON°+1
DJF°+2

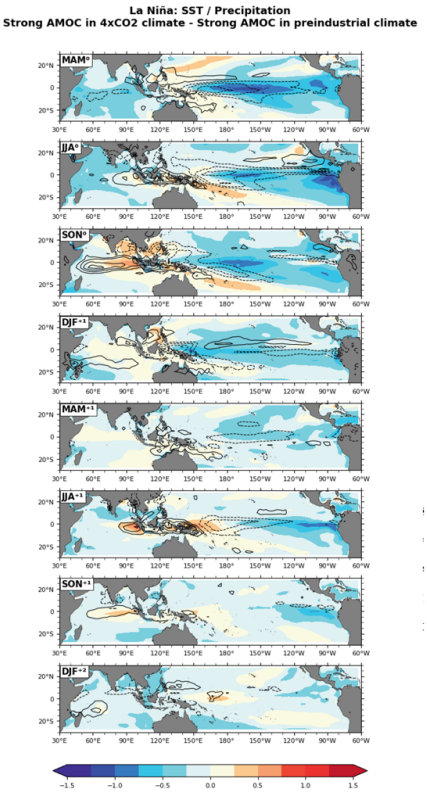
La Niña: SST / Precipitation
Strong AMOC in 4xCO2 climate - Strong AMOC in preindustrial climate
MAM°
JJA°
SON°
DJF°+1
MAM°+1
JJA°+1
SON°+1
DJF°+2

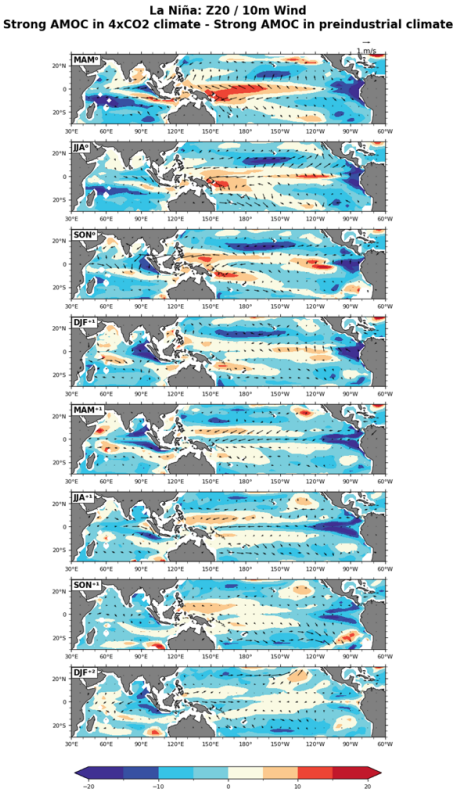
La Niña: Z20 / 10m Wind
Strong AMOC in 4xCO2 climate - Strong AMOC in preindustrial climate
MAM°
JJA°
SON°
DJF°+1
MAM°+1
JJA°+1
SON°+1
DJF°+2

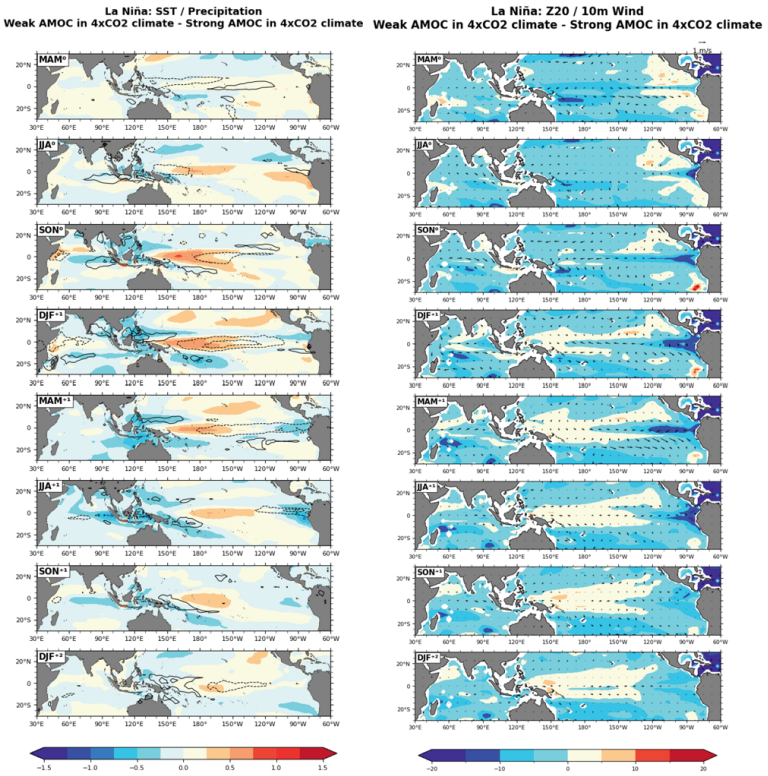

Figure 5.18: La Niña seasonal composite evolution differences across EC-Earth3 experiments starting in MAM^0 and ending in DJF^{+2} for (left) SST and precipitation anomalies and (right) thermocline depth (Z20) and 10m wind anomalies. SST (°C) and Z20 (m) are shaded; precipitation contours (solid for positive differences, dashed for negative differences) are ±5, ±4, ±3, ±2, ±1 mm/day, and the wind vector scale (m/s) is shown at the top of the figure.

Chapter 6

Discussion

This chapter provides a comprehensive interpretation of the simulation results, situating them within the broader scientific debate surrounding the complex and often contested relationship between AMOC and ENSO.
A necessary first step in this interpretation is the assessment of EC-Earth3's ability to simulate ENSO dynamics. The analyses confirm that EC-Earth3 successfully reproduces the main climatological features of the tropical Pacific, including the meridional and zonal SST gradients, the extent of the western Pacific warm pool, and the equatorial cold tongue. The model also captures the spatial pattern of interannual SST variability, with maxima along the cold tongue broadly consistent with observations. Furthermore, the timing of the Niño-3.4 index seasonal cycle and the dominant 3-5 year periodicity characteristic of ENSO are realistically represented. Autocorrelation analyses confirm that EC-Earth3 reproduces the typical phase evolution and temporal persistence of ENSO events, while the spectral analysis demonstrates that the main interannual timescales are captured.
Despite this overall fidelity, systematic biases remain. EC-Earth3 exhibits a warm SST bias in the western Pacific and along the South American coast, while underestimating SSTs in the central equatorial Pacific. The amplitude of both El Niño and La Niña events is generally lower than observed, as indicated by the reduced standard deviations of SST anomalies, the flatter Niño-3.4 power spectrum, and the composite analyses. Moreover, cold anomalies associated with La Niña tend to decay more rapidly, leading to shorter event persistence than in observations.

Collectively, these features indicate that EC-Earth3 produces an ENSO that is weaker, more symmetric, and less temporally persistent than observed.
The findings of Yang et al. (2019) closely align with the present analysis. In their assessment of EC-Earth3, they identify the same pattern of biases: an underestimation of ENSO amplitude and interannual variability compared to HadISST observations, along with a symmetric response between El Niño and La Niña. They suggest that these biases originate from the model's mean-state SST errors in the Tropical Pacific, particularly the presence of warm anomalies in the western basin and cold biases in the central equatorial Pacific, which weaken the strength of atmosphere-ocean coupling. Their experiments further demonstrate that incorporating stochastic physics into the atmospheric component increases both the amplitude and variability of ENSO, improving especially the strength and asymmetry of the events. Comparisons with other coupled models further contextualize these findings. Deser et al. (2012) evaluated the representation of ENSO in the CCSM4 model and found that, while it realistically reproduces the spatial structure, seasonal evolution and, crucially, ENSO asymmetry, it substantially overestimates the amplitude by approximately 30%. This behavior reflects an overly strong ocean–atmosphere coupling, leading to an excessively vigorous ENSO system. In contrast, both the present analysis and Yang et al. (2019) show that EC-Earth3 produces a weaker and more symmetric ENSO with reduced amplitude and variability. Yang et al. explicitly compared EC-Earth3 with CCSM and confirmed this contrast, attributing it to opposite mean-state biases in the tropical Pacific: while EC-Earth3's warm western Pacific weakens coupled feedbacks, the cooler and drier eastern Pacific in CCSM excessively amplifies ENSO. These contrasting behaviors illustrate how coupled models can achieve broadly realistic ENSO dynamics through compensating errors in the mean tropical Pacific state and in the strength of atmosphere-ocean coupling.
Moving on to the simulations analysis, the investigation of the impacts of a weakened AMOC under preindustrial conditions reveals a modest and spatially complex response in the ENSO system. The analysis indicates that an AMOC slowdown does not produce a uniform amplification or suppression of ENSO. Instead, it induces a nuanced reorganization of its spatial structure, seasonal cycle, and event characteristics. At the basin-scale, the response to a weakened AMOC is dominated

by the well-documented interhemispheric temperature dipole, with widespread cooling across the Northern Hemisphere and moderate warming in the Southern Hemisphere. Within this altered mean state, the variability of SST anomalies exhibits a complex pattern: a modest increase occurs in the eastern equatorial Pacific, partially offset by a slight decrease toward the central and western Pacific. This spatial heterogeneity explains why the net impact on the Niño 3.4 index, which integrates SST anomalies over a broad central-eastern Pacific domain, is minimal. The annual standard deviation of the index increases only marginally, while the seasonal distribution shows subtle changes, with variability slightly increasing from late boreal winter to early summer and decreasing from late summer through early winter. The power spectrum analysis reveals that the dominant 3-5 year ENSO periodicity remains essentially unchanged by the AMOC slowdown. However, a slight increase in spectral power within this band indicates a tendency toward a modest amplification of ENSO event amplitude. This is consistent with the observed reduction in the amplitude of the seasonal SST cycle in the Niño 3.4 region, a mechanism previously linked to stronger ENSO excursions. The composite analysis of ENSO events further clarifies these changes. For El Niño events, a weakened AMOC leads to warmer SST anomalies that are more intense and concentrated in the eastern Pacific. Coupled field analyses confirm an amplified and prolonged canonical El Niño response, with intensified eastern-Pacific warming accompanied by enhanced convective precipitation and a more pronounced flattening of the thermocline. In contrast, La Niña events are only weakly affected. The main effect appears to be a slight decrease and a shift in the timing of the event's onset, with cold anomalies developing earlier and more abruptly compared to the strong-AMOC case. However, the overall intensity and spatial structure of La Niña remain largely unchanged, and the coupled atmosphere-ocean fields show minimal systematic modifications.

The modest and asymmetric nature of the ENSO response identified in this analysis occupies an intermediate position within a scientific literature characterized by divergent findings. The results align with certain aspects of previous studies while conflicting with others, reinforcing the hypothesis that the AMOC-ENSO teleconnection is highly sensitive to model physics. A prominent group of studies

has concluded that an AMOC slowdown robustly amplifies ENSO. Using a multi-model ensemble, Timmermann et al. (2007) found a significant intensification of ENSO variability in all five models analyzed. Similarly, Dong & Sutton (2007) reported a marked 36% increase in the Niño-3 index standard deviation following an AMOC collapse. Both studies, along with Molina et al. (2022), attributed this amplification primarily to a weakening of the seasonal cycle in the tropical Pacific, which allows for larger interannual fluctuations through a mechanism of nonlinear frequency entrainment. The results presented herein are qualitatively consistent with this mechanism, as a weakened seasonal cycle is also found to co-occur with a slight increase in ENSO amplitude. However, the magnitude of this amplification is vastly smaller than that reported by Dong & Sutton.

Conversely, the finding of a near-neutral change in overall ENSO amplitude resonates with the work of Williamson et al. (2017). Using a high-resolution model, they found that ENSO amplitude remained essentially unchanged after an AMOC collapse, an effect attributed to compensating interactions between reduced oceanic damping and decreased stochastic atmospheric forcing. Furthermore, the eastward intensification of El Niño anomalies in the present experiment is consistent with the eastward shift in the ENSO pattern they observed. These findings stand in direct opposition to the damping effect reported by Orihuela-Pinto et al. (2022). Their study concluded that an AMOC collapse led to a ~30% decrease in ENSO variability, driven by a cooler tropical Pacific and a strengthened Walker circulation that suppressed the Bjerknes feedback. It is noteworthy that Orihuela-Pinto et al. also simulated a weakened Pacific annual cycle, but in their model, this did not lead to ENSO amplification, highlighting that other mean-state changes can override the nonlinear entrainment mechanism.

Taken together, these divergent outcomes underscore the complexity of the AMOC-ENSO teleconnection. The modest, spatially complex, and asymmetric response found in EC-Earth3 suggests that the lack of consensus in the literature may arise from the intrinsically non-robust nature of this long-range interaction. The moderate response in this experiment could reflect a less abrupt forcing compared to the full AMOC collapse simulated in other studies, highlighting a strong dependence on the experimental design. Ultimately, these findings suggest that the outcome is determined by a delicate balance between competing mechanisms, such as the

weakening of the seasonal cycle, changes in the Bjerknes feedback, and shifts in atmospheric forcing, whose relative importance varies significantly across different climate models.

A central objective of this thesis is to determine whether the AMOC-ENSO teleconnection is state-dependent. To this end, the analysis is extended to a high-emission ($4xCO_2$) climate scenario. Before assessing the specific impact of AMOC weakening in this warmer world, it is first necessary to isolate the influence of the greenhouse forcing itself by comparing the strong-AMOC simulations under both preindustrial and $4xCO_2$ conditions. The application of a strong radiative forcing produces substantial changes in the tropical Pacific mean state and variability, even with the AMOC maintained at a preindustrial-like strength. The climatological mean state warms significantly across the basin, with the most pronounced temperature increase occurring in the eastern equatorial cold tongue. This leads to a marked reduction in the zonal SST gradient, a fundamental feature of the Pacific mean state. Within this altered background, ENSO variability intensifies significantly. The standard deviation of SST anomalies increases across the central equatorial Pacific, and the power spectrum of the Niño 3.4 index shows a substantial increase in energy within the canonical 3–5 year ENSO band. This amplification is most pronounced during the boreal autumn and winter, reinforcing the seasonal phase-locking of a more energetic ENSO cycle. Composite analyses further reveal that El Niño events become stronger and broader, with positive SST anomalies extending farther west toward the dateline. This westward expansion of both the anomaly pattern and the center of maximum variability suggests a shift toward more Central-Pacific type events.

The simulated amplification of ENSO under strong greenhouse forcing is consistent with the findings of Yang et al. (2019), who analyzed the same EC-Earth3 model under the RCP8.5 scenario. Their simulation for a global warming world similarly produced stronger El Niño and La Niña events compared to historical experiments, along with a more energetic and sharply peaked power spectrum. This corroborates the result that, within this model, a warmer background climate fosters a more vigorous ENSO system. More importantly, Yang et al's investigation into the role of stochastic physics provides compelling support for this work's central hypothesis that the ENSO response is inherently state-dependent. They showed

that incorporating stochastic atmospheric forcing amplified ENSO variability in the historical climate but slightly damped it in the warmer RCP8.5 world. This reversal indicates that the altered mean state of the tropical Pacific under greenhouse forcing fundamentally modifies the system's sensitivity to internal perturbations. While Yang et al. demonstrated that the background climate state modulates the ENSO response to stochastic atmospheric noise, the results presented here show that it likewise governs the response to a large-scale oceanic perturbation such as an AMOC slowdown.

This state-dependent framework is therefore essential for addressing the central question of this work: how does a concurrent AMOC slowdown modify the ENSO response in this altered, warmer climate? The comparison between the weak- and strong-AMOC experiments in the $4xCO_2$ climate reveals a fundamental shift in the teleconnection's role. In contrast to the preindustrial scenario, where it acted as a minor and selective amplifier, in a warmer world, a weakened AMOC acts as a negative feedback, partially counteracting the greenhouse-gas-driven intensification of ENSO. This moderating influence is evident across multiple diagnostics. The overall ENSO variability, while remaining well above preindustrial levels, is slightly reduced in the weak-AMOC simulation compared to its strong-AMOC counterpart. The power spectrum of the Niño 3.4 index shows a discernible decrease in energy, and the annual cycle of its standard deviation is similarly damped. Spatially, the AMOC slowdown reverses the westward expansion of variability induced by global warming. The zone of maximum SST variability contracts, becoming more pronounced in the eastern Pacific, suggesting a reorganization of ENSO dynamics back toward a more canonical, eastern-Pacific-focused pattern. The composite analyses for El Niño and La Niña events confirm this state-dependent behavior. For El Niño, an AMOC weakening in the $4xCO_2$ climate dampens the event's amplitude in the central Pacific, the very region where greenhouse forcing caused the strongest amplification. The result is a more spatially confined warming pattern that is shifted eastward relative to the strong-AMOC case. This indicates that the AMOC slowdown directly counteracts the tendency of global warming to produce broader, more Central Pacific-type El Niño events. The impact on La Niña is qualitatively similar, though less pronounced.

The finding that an AMOC slowdown exerts a damping influence on ENSO in a

high-CO_2 world stands in partial contrast to the recent work of Liu et al. (2023), who also investigated this teleconnection under anthropogenic warming using the CCSM4 model. Their study concluded that a weakened AMOC strengthens ENSO variability by approximately 11% throughout the twenty-first century. The discrepancy originates from the models' fundamentally different baseline responses to greenhouse forcing. In the CCSM4 simulation used by Liu et al., anthropogenic warming alone leads to a modest reduction in ENSO variability. Therefore, the 11% strengthening induced by the AMOC slowdown acts to partially counteract this baseline damping effect. In contrast, the EC-Earth3 model shows a strong amplification of ENSO under 4xCO_2 forcing. The damping effect of the AMOC slowdown in the present study therefore also acts in opposition to the baseline trend. Consequently, both studies portray the AMOC slowdown as a negative feedback that pushes against the primary trend induced by greenhouse warming. Furthermore, the studies diverge on the impact on ENSO's spatial structure. Liu et al. found that a weakened AMOC promotes a higher frequency of Central Pacific El Niño events. The present analysis shows the opposite: AMOC weakening reverses the westward shift induced by warming, causing a return to a more canonical, Eastern-Pacific-focused pattern. These contrasting outcomes, obtained from two state-of-the-art climate models, underscore the conclusion that there is no simple, universal response of ENSO to an AMOC slowdown in a warming climate. The teleconnection is highly sensitive to model-specific mean states and feedback processes.

Chapter 7

Conclusions

This thesis investigated the relationship between the AMOC and ENSO, with a specific focus on how this complex and often contested interaction changes in a warmer climate. Using the EC-Earth3 climate model, four targeted experiments were analyzed, combining two climate states (preindustrial and 4xCO_2) with two AMOC regimes (strong and weak), to systematically dissect their coupled behavior. The key findings reveal a teleconnection that is fundamentally dependent on the background climate state. Under preindustrial conditions, a weakened AMOC induces a weak, complex, and asymmetric response in ENSO, selectively amplifying El Niño events, particularly in the eastern Pacific, while leaving La Niña events largely unchanged. As a result, the net effect on ENSO variability is minimal. In a high-CO_2 climate, the dynamics shift fundamentally. Greenhouse forcing in isolation acts as a powerful amplifier of ENSO, fostering more vigorous events with a westward-shifted spatial footprint. The central and most significant finding of this work is that a concurrent AMOC slowdown in this warmer world acts as a negative feedback. It partially counteracts the greenhouse-gas-driven intensification of ENSO by moderating its amplitude and, crucially, reversing its westward expansion, causing a return to a more canonical, Eastern-Pacific-focused pattern.

The main conclusion of this thesis is the demonstration that the impact of the AMOC on ENSO is profoundly state-dependent. The teleconnection's role shifts from that of a marginal and selective amplifier in a preindustrial world to a significant modulator that opposes the primary effects of greenhouse forcing in a

high-CO_2 climate. This finding has critical implications, suggesting that future projections of ENSO variability and its associated global climate impacts cannot be reliably made without accounting for the concurrent, and widely projected, slowdown of the AMOC.

These conclusions, however, are based on simulations from a single model. Although the EC-Earth3 model's performance was evaluated as credible for representing the core dynamics of ENSO, its intrinsic biases, such as a slightly underestimated ENSO amplitude and reduced La Niña persistence, could influence the results. To confirm the robustness of these findings, a coordinated multi-model intercomparison project employing a similar experimental design is a necessary next step. Improving a single model to capture all aspects of ENSO remains a significant challenge, as adjustments to one physical process often disrupt others. Therefore, a practical path forward may lie in combining different models to leverage their individual strengths while minimizing weaknesses. Future work should also prioritize applying this experimental framework to large ensemble simulations, as studies suggest that ensembles of 50 or more members are needed to robustly capture baseline ENSO characteristics (Lee et al., 2021).

As the Earth system continues its trajectory into an unprecedented climatic state, understanding how its fundamental modes of variability, such as AMOC and ENSO, will co-evolve remains a fundamental question for climate science. This work represents a step toward unraveling that complexity, highlighting that the relationships of the past may not be a reliable guide for the future.

References

Alexander, M. A., Bladé, I., Newman, M., Lanzante, J. R., Lau, N.-C., Scott, J. D. (2002). The Atmospheric Bridge: The Influence of ENSO Teleconnections on Air–Sea Interaction over the Global Oceans. Journal of Climate, 15(16), 2205–2231. https://doi.org/10.1175/1520-0442(2002)015<2205:TABTIO>2.0.CO;2

Alizadeh, O. (2022). A review of the El Niño-Southern Oscillation in future. Earth-Science Reviews, 235, 104246. https://doi.org/10.1016/j.earscirev.2022.104246

Ashok, K., Behera, S. K., Rao, S. A., Weng, H., Yamagata, T. (2007). El Niño Modoki and its possible teleconnection. Journal of Geophysical Research: Oceans, 112(C11). https://doi.org/10.1029/2006JC003798

Bellomo, K., Angeloni, M., Corti, S., von Hardenberg, J. (2021). Future climate change shaped by inter-model differences in Atlantic meridional overturning circulation response. Nature Communications, 12(1), 3659. https://doi.org/10.1038/s41467-021-24015-w

Bellomo, K., Meccia, V. L., D'Agostino, R., Fabiano, F., Larson, S. M., von Hardenberg, J., Corti, S. (2023). Impacts of a weakened AMOC on precipitation over the Euro-Atlantic region in the EC-Earth3 climate model. Climate Dynamics, 61(7), 3397–3416. https://doi.org/10.1007/s00382-023-06754-2

Bellomo, K., Mehling, O. (2024). Impacts and State-Dependence of AMOC Weakening in a Warming Climate. Geophysical Research Letters, 51(10), e2023GL107624. https://doi.org/10.1029/2023GL107624

Bjerknes, J. (1969). Atmospheric Teleconnections from the Equatorial Pacific. Monthly Weather Review, 97(3), 163–172. https://doi.org/10.1175/1520-0493(1969)097<0163:ATFTEP>2.3.CO;2

Brodeau, L., Koenigk, T. (2016). Extinction of the northern oceanic deep convection in an ensemble of climate model simulations of the 20th and 21st centuries. Climate Dynamics, 46(9), 2863–2882. https://doi.org/10.1007/s00382-015-2736-5

Caesar, L., McCarthy, G. D., Thornalley, D. J. R., Cahill, N., Rahmstorf, S. (2021). Current Atlantic Meridional Overturning Circulation weakest in last millennium. Nature Geoscience, 14(3), 118–120. https://doi.org/10.1038/s41561-021-00699-z

Cai, W., Ng, B., Geng, T., Jia, F., Wu, L., Wang, G., Liu, Y., Gan, B., Yang, K., Santoso, A., Lin, X., Li, Z., Liu, Y., Yang, Y., Jin, F.-F., Collins, M., McPhaden, M. J. (2023). Anthropogenic impacts on twentieth-century ENSO variability changes. Nature Reviews Earth Environment, 4(6), 407–418. https://doi.org/10.1038/s43017-023-00427-8

Capotondi, A., Sardeshmukh, P. D. (2017). Is El Niño really changing? Geophysical Research Letters, 44(16), 8548–8556. https://doi.org/10.1002/2017GL074515

Capotondi, A., Wittenberg, A. T., Newman, M., Lorenzo, E. D., Yu, J.-Y., Braconnot, P., Cole, J., Dewitte, B., Giese, B., Guilyardi, E., Jin, F.-F., Karnauskas, K., Kirtman, B., Lee, T., Schneider, N., Xue, Y., Yeh, S.-W. (2015). Understanding ENSO Diversity. Bulletin of the American Meteorological Society, 96(6), 921–938. https://doi.org/10.1175/BAMS-D-13-00117.1

Change (IPCC), I. P. on C. (2022). Extremes, Abrupt Changes and Managing Risks. In The Ocean and Cryosphere in a Changing Climate: Special Report of the Intergovernmental Panel on Climate Change (pp. 589–656). Cambridge University Press.

Deser, C., Phillips, A. S., Tomas, R. A., Okumura, Y. M., Alexander, M. A.,

Capotondi, A., Scott, J. D., Kwon, Y.-O., Ohba, M. (2012). ENSO and Pacific Decadal Variability in the Community Climate System Model Version 4. Journal of Climate, 25(8), 2622–2651. https://doi.org/10.1175/JCLI-D-11-00301.1

Deser, C., Simpson, I. R., McKinnon, K. A., Phillips, A. S. (2017). The Northern Hemisphere Extratropical Atmospheric Circulation Response to ENSO: How Well Do We Know It and How Do We Evaluate Models Accordingly? Journal of Climate, 30(13), 5059–5082. https://doi.org/10.1175/JCLI-D-16-0844.1

Dong, B., Sutton, R. T. (2007). Enhancement of ENSO Variability by a Weakened Atlantic Thermohaline Circulation in a Coupled GCM. Journal of Climate, 20(19), 4920–4939. https://doi.org/10.1175/JCLI4284.1

Döscher, R., Acosta, M., Alessandri, A., Anthoni, P., Arsouze, T., Bergman, T., Bernardello, R., Boussetta, S., Caron, L.-P., Carver, G., Castrillo, M., Catalano, F., Cvijanovic, I., Davini, P., Dekker, E., Doblas-Reyes, F. J., Docquier, D., Echevarria, P., Fladrich, U., ... Zhang, Q. (2022). The EC-Earth3 Earth system model for the Coupled Model Intercomparison Project 6. Geoscientific Model Development, 15(7), 2973–3020. https://doi.org/10.5194/gmd-15-2973-2022

Feulner, G., Rahmstorf, S., Levermann, A., Volkwardt, S. (2013). On the Origin of the Surface Air Temperature Difference between the Hemispheres in Earth's Present-Day Climate. Journal of Climate, 26(18), 7136–7150. https://doi.org/10.1175/JCLI-D-12-00636.1

Fredriksen, H.-B., Berner, J., Subramanian, A. C., Capotondi, A. (2020). How Does El Niño–Southern Oscillation Change Under Global Warming—A First Look at CMIP6. Geophysical Research Letters, 47(22), e2020GL090640. https://doi.org/10.1029/2020GL090640

Geng, T., Cai, W., Jia, F., Wu, L. (2024). Decreased ENSO post-2100 in response to formation of a permanent El Niño-like state under greenhouse warming. Nature Communications, 15(1), 5810. https://doi.org/10.1038/s41467-024-50156-9

Gierz, P., Lohmann, G., Wei, W. (2015). Response of Atlantic overturning

to future warming in a coupled atmosphere-ocean-ice sheet model. Geophysical Research Letters, 42(16), 6811–6818. https://doi.org/10.1002/2015GL065276

Hersbach, H., Bell, B., Berrisford, P., Hirahara, S., Horányi, A., Muñoz-Sabater, J., Nicolas, J., Peubey, C., Radu, R., Schepers, D., Simmons, A., Soci, C., Abdalla, S., Abellan, X., Balsamo, G., Bechtold, P., Biavati, G., Bidlot, J., Bonavita, M., ... Thépaut, J.-N. (2020). The ERA5 global reanalysis. Quarterly Journal of the Royal Meteorological Society, 146(730), 1999–2049. https://doi.org/10.1002/qj.3803

Hu, A., Richter, I., Okumura, Y., Burls, N., Keenlyside, N., Parfitt, R., Bellomo, K., Bellucci, A., Farneti, R., Fedorov, A. V., Ferster, B. S., He, C., Li, Q., Matei, D. (2025). Unraveling the Complexity of Global Climate Dynamics: Interactions among El Niño–Southern Oscillation, Atlantic Meridional Overturning Circulation, and Tropical Basins Across Different Timescales. Ocean-Land-Atmosphere Research, 4, 0096. https://doi.org/10.34133/olar.0096

Huang, B., Thorne, P. W., Banzon, V. F., Boyer, T., Chepurin, G., Lawrimore, J. H., Menne, M. J., Smith, T. M., Vose, R. S., Zhang, H.-M. (2017). Extended Reconstructed Sea Surface Temperature, Version 5 (ERSSTv5): Upgrades, Validations, and Intercomparisons. Journal of Climate, 30(20), 8179–8205. https://doi.org/10.1175/JCLI-D-16-0836.1

IPCC, I. P. on C. (2021). Technical Summary. In Climate Change 2021 – The Physical Science Basis: Working Group I Contribution to the Sixth Assessment Report of the Intergovernmental Panel on Climate Change (pp. 35–144). Cambridge University Press.

Jackson, L. C., Kahana, R., Graham, T., Ringer, M. A., Woollings, T., Mecking, J. V., Wood, R. A. (2015). Global and European climate impacts of a slowdown of the AMOC in a high resolution GCM. Climate Dynamics, 45(11), 3299–3316. https://doi.org/10.1007/s00382-015-2540-2

Johnson, N. C. (2013). How Many ENSO Flavors Can We Distinguish? Journal of Climate, 26(13), 4816–4827. https://doi.org/10.1175/JCLI-D-12-00649.1

Lan, X., Tans, P., Thoning, K. W. (2025). Trends in globally-averaged CO

determined from NOAA Global Monitoring Laboratory measurements. NOAA. https://doi.org/10.15138/9N0H-ZH07

Lean, J. L., Rind, D. H. (2008). How natural and anthropogenic influences alter global and regional surface temperatures: 1889 to 2006. Geophysical Research Letters, 35(18). https://doi.org/10.1029/2008GL034864

Lee, J., Planton, Y. Y., Gleckler, P. J., Sperber, K. R., Guilyardi, E., Wittenberg, A. T., McPhaden, M. J., Pallotta, G. (2021). Robust Evaluation of ENSO in Climate Models: How Many Ensemble Members Are Needed? Geophysical Research Letters, 48(20), e2021GL095041. https://doi.org/10.1029/2021GL095041

Lenton, T. M., Milkoreit, M., Willcock, S., Abrams, J. F., Armstrong McKay, D. I., Buxton, J. E., Donges, J. F., Loriani, S., Wunderling, N., Alkemade, F., Barrett, M., Constantino, S., Powell, T., Smith, S. R., Boulton, C. A., Pinho, P., Dijkstra, H. A. Pearce-Kelly, P., RomanCuesta, R. M., Dennis, D. (eds), 2025, The Global Tipping Points Report 2025. University of Exeter, Exeter, UK. ©The Global Tipping Points Report 2025, University of Exeter, UK

Liu, W., Duarte Cavalcante Pinto, D., Fedorov, A., Zhu, J. (2023). The Impacts of a Weakened Atlantic Meridional Overturning Circulation on ENSO in a Warmer Climate. Geophysical Research Letters, 50(8), e2023GL103025. https://doi.org/10.1029/2023GL103025

Lynch-Stieglitz, J. (2017). The Atlantic Meridional Overturning Circulation and Abrupt Climate Change. Annual Review of Marine Science, 9, 83–104. https://doi.org/10.1146/annurev-marine-010816-060415

Marshall, J., Donohoe, A., Ferreira, D., McGee, D. (2014). The ocean's role in setting the mean position of the Inter-Tropical Convergence Zone. Climate Dynamics, 42(7), 1967–1979. https://doi.org/10.1007/s00382-013-1767-z

McCarthy, G. D., Hug, G., Smeed, D., Morris, K. J., Moat, B. (2025). Signal and Noise in the Atlantic Meridional Overturning Circulation at 26°N. Geophysical Research Letters, 52(7), e2025GL115055. https://doi.org/10.1029/2025GL115055

Molina, M. J., Hu, A., Meehl, G. A. (2022). Response of Global SSTs and ENSO to the Atlantic and Pacific Meridional Overturning Circulations. Journal of Climate, 35(1), 49–72. https://doi.org/10.1175/JCLI-D-21-0172.1

NOAA. (2014). Climate Models. Climate.gov. https://www.climate.gov/maps-data/climate-data-primer/predicting-climate/climate-models

OCHA. (2017). OCHA Annual Report 2016. https://digitallibrary.un.org/record/4048391

Okumura, Y. M., Deser, C. (2010). Asymmetry in the Duration of El Niño and La Niña. Journal of Climate, 23(21), 5826–5843. https://doi.org/10.1175/2010JCLI3592.1

O'Neill, B. C., Tebaldi, C., van Vuuren, D. P., Eyring, V., Friedlingstein, P., Hurtt, G., Knutti, R., Kriegler, E., Lamarque, J.-F., Lowe, J., Meehl, G. A., Moss, R., Riahi, K., Sanderson, B. M. (2016). The Scenario Model Intercomparison Project (ScenarioMIP) for CMIP6. Geoscientific Model Development, 9(9), 3461–3482. https://doi.org/10.5194/gmd-9-3461-2016

Orihuela-Pinto, B., Santoso, A., England, M. H., Taschetto, A. S. (2022). Reduced ENSO Variability due to a Collapsed Atlantic Meridional Overturning Circulation. Journal of Climate, 35(16), 5307–5320. https://doi.org/10.1175/JCLI-D-21-0293.1

Power, S., Kociuba, G. (2010). The impact of global warming on the Southern Oscillation Index. Climate Dynamics, 37, 1745–1754. https://doi.org/10.1007/s00382-010-0951-7

Rasmusson, E. M., Carpenter, T. H. (1982). Variations in Tropical Sea Surface Temperature and Surface Wind Fields Associated with the Southern Oscillation/El Niño. Monthly Weather Review, 110(5), 354–384. https://doi.org/10.1175/1520-0493(1982)110<0354:VITSST>2.0.CO;2

Rayner, N. A., Parker, D. E., Horton, E. B., Folland, C. K., Alexander, L. V., Rowell, D. P., Kent, E. C., Kaplan, A. (2003). Global analyses of sea

surface temperature, sea ice, and night marine air temperature since the late nineteenth century. Journal of Geophysical Research: Atmospheres, 108(D14). https://doi.org/10.1029/2002JD002670

Ropelewski, C. F., Halpert, M. S. (1987). Global and Regional Scale Precipitation Patterns Associated with the El Niño/Southern Oscillation. Monthly Weather Review, 115(8), 1606–1626. https://doi.org/10.1175/1520-0493(1987)115<1606:GARSPP>2.0.CO;2

Stevenson, S., Fox-Kemper, B., Jochum, M., Rajagopalan, B., Yeager, S. G. (2010). ENSO Model Validation Using Wavelet Probability Analysis. Journal of Climate, 23(20), 5540–5547. https://doi.org/10.1175/2010JCLI3609.1

Stewart, R. H. (2008). Introduction to Physical Oceanography.

Stommel, H. (1961). Thermohaline Convection with Two Stable Regimes of Flow. Tellus, 13(2), 224–230. https://doi.org/10.1111/j.2153-3490.1961.tb00079.x

Timmermann, A., Okumura, Y., An, S.-I., Clement, A., Dong, B., Guilyardi, E., Hu, A., Jungclaus, J. H., Renold, M., Stocker, T. F., Stouffer, R. J., Sutton, R., Xie, S.-P., Yin, J. (2007). The Influence of a Weakening of the Atlantic Meridional Overturning Circulation on ENSO. Journal of Climate, 20(19), 4899–4919. https://doi.org/10.1175/JCLI4283.1

Toggweiler, J. R., Samuels, B. (1995). Effect of drake passage on the global thermohaline circulation. Deep Sea Research Part I: Oceanographic Research Papers, 42(4), 477–500. https://doi.org/10.1016/0967-0637(95)00012-U

Trenberth, K. E. (1997). The Definition of El Niño. Bulletin of the American Meteorological Society, 78(12), 2771–2778. https://doi.org/10.1175/1520-0477(1997)078<2771:TDOENO>2.0.CO;2

Wang, C. (2018). A review of ENSO theories. National Science Review, 5. https://doi.org/10.1093/nsr/nwy104

Wang, C., Deser, C., Yu, J.-Y., Clement, A. (2017). El Niño and Southern Oscillation (ENSO): A review (Vol. 8, pp. 85–106). https://doi.org/10.1007/978-94-017-7499-4_4

Wang, C., Picaut, J. (2004). Understanding Enso Physics—A Review. In Earth's Climate (pp. 21–48). American Geophysical Union (AGU). https://doi.org/10.1029/147GM02

Wang, J., Fang, X., Chen, N., Qin, B., Mu, M., Ji, C. (2025). A dual-core model for ENSO diversity: Unifying model hierarchies for realistic simulations. Npj Climate and Atmospheric Science, 8(1), 269. https://doi.org/10.1038/s41612-025-01164-z

Weijer, W., Cheng, W., Drijfhout, S. S., Fedorov, A. V., Hu, A., Jackson, L. C., Liu, W., McDonagh, E. L., Mecking, J. V., Zhang, J. (2019). Stability of the Atlantic Meridional Overturning Circulation: A Review and Synthesis. Journal of Geophysical Research: Oceans, 124(8), 5336–5375. https://doi.org/10.1029/2019JC015083

Weijer, W., Cheng, W., Garuba, O. A., Hu, A., Nadiga, B. T. (2020). CMIP6 Models Predict Significant 21st Century Decline of the Atlantic Meridional Overturning Circulation. Geophysical Research Letters, 47(12), e2019GL086075. https://doi.org/10.1029/2019GL086075

Williamson, M., Collins, M., Drijfhout, S., Kahana, R., Mecking, J., Lenton, T. (2018). Effect of AMOC collapse on ENSO in a high resolution general circulation model. Climate Dynamics, 50, 1–16. https://doi.org/10.1007/s00382-017-3756-0

Worthington, E. L., Moat, B. I., Smeed, D. A., Mecking, J. V., Marsh, R., McCarthy, G. D. (2021). A 30-year reconstruction of the Atlantic meridional overturning circulation shows no decline. Ocean Science, 17(1), 285–299. https://doi.org/10.5194/os-17-285-2021

Yang, C., Christensen, H. M., Corti, S., von Hardenberg, J., Davini, P. (2019).

The impact of stochastic physics on the El Niño Southern Oscillation in the EC-Earth coupled model. Climate Dynamics, 53(5), 2843–2859. https://doi.org/10.1007/s00382-019-04660-0

Yeh, S.-W., Kug, J.-S., Dewitte, B., Kwon, M.-H., Kirtman, B. P., Jin, F.-F. (2009). El Niño in a changing climate. Nature, 461(7263), 511–514. https://doi.org/10.1038/nature08316

Zhang, R., Delworth, T. L. (2005). Simulated Tropical Response to a Substantial Weakening of the Atlantic Thermohaline Circulation. Journal of Climate, 18(12), 1853–1860. https://doi.org/10.1175/JCLI3460.1